

Deep sr-DDL: Deep Structurally Regularized Dynamic Dictionary Learning to Integrate Multimodal and Dynamic Functional Connectomics data for Multidimensional Clinical Characterizations

N.S. D'Souza^{a,*}, M.B. Nebel^{b,c}, D. Crocetti^b, J. Robinson^b, N. Wymbs^{b,c}, S.H. Mostofsky^{b,c,d}, A. Venkataraman^a

^aDepartment of Electrical and Computer Engineering, Johns Hopkins University, USA

^bCenter for Neurodevelopmental & Imaging Research, Kennedy Krieger Institute, USA

^cDepartment of Neurology, Johns Hopkins School of Medicine, USA

^dDepartment of Psychiatry and Behavioral Science, Johns Hopkins School of Medicine, USA

Abstract

We propose a novel integrated framework that jointly models complementary information from resting-state functional MRI (rs-fMRI) connectivity and diffusion tensor imaging (DTI) tractography to extract biomarkers of brain connectivity predictive of behavior. Our framework couples a generative model of the connectomics data with a deep network that predicts behavioral scores. The generative component is a structurally-regularized Dynamic Dictionary Learning (sr-DDL) model that decomposes the dynamic rs-fMRI correlation matrices into a collection of shared basis networks and time varying subject-specific loadings. We use the DTI tractography to regularize this matrix factorization and learn anatomically informed functional connectivity profiles. The deep component of our framework is an LSTM-ANN block, which uses the temporal evolution of the subject-specific sr-DDL loadings to predict multidimensional clinical characterizations. Our joint optimization strategy collectively estimates the basis networks, the subject-specific time-varying loadings, and the neural network weights. We validate our framework on a dataset of neurotypical individuals from the Human Connectome Project (HCP) database to map to cognition and on a separate multi-score prediction task on individuals diagnosed with Autism Spectrum Disorder (ASD) in a five-fold cross validation setting. Our hybrid model outperforms several state-of-the-art approaches at clinical outcome prediction and learns interpretable multimodal neural signatures of brain organization.

Keywords: Dynamic Dictionary Learning, Structural Regularization, Multimodal Integration, Functional Magnetic Resonance Imaging, Diffusion Tensor Imaging, Clinical Severity

1. Introduction

Functional magnetic resonance imaging (fMRI) quantifies the changes in blood flow and oxygenation in the regions associated with neuronal activity. More specifically, resting state fMRI (rs-fMRI) is acquired in the absence of a task paradigm, thus allowing us to probe the spontaneous co-activation patterns in the brain. It is believed that the co-activations reflect the intrinsic functional connectivity between brain regions [Fox and Raichle (2007)]. In contrast to fMRI, Diffusion Tensor Imaging (DTI) [Assaf and Pasternak (2008)] assesses structural connectivity by measuring the diffusion of water molecules across neuronal fibres in the brain. Going one step further, we can use tractography to construct detailed 3D maps of anatomical pathways within the brain based on the diffusion tensors. There is strong evidence in literature of the correspondence between functional and structural pathways within

the brain [Skudlarski, Jagannathan, Calhoun, Hampson, Skudlarska and Pearlson (2008)], with several studies suggesting that this functional connectivity may be mediated by either direct or indirect anatomical connections [Atasoy, Donnelly and Pearson (2016); Bowman, Zhang, Derado and Chen (2012); Fukushima, Betzel, He, van den Heuvel, Zuo and Sporns (2018); Honey, Sporns, Cammoun, Gigandet, Thiran, Meuli and Hagmann (2009)]. Thus, rs-fMRI and DTI data provide complementary information about function and structure respectively, which when integrated together can be used to construct a more comprehensive view of brain organization both in health and disease. As a result, multimodal integration has become an important topic of study for the characterization of neuropsychiatric disorders such as Autism Spectrum Disorder (ASD) [Visser, Cohen and Geurts (2012)], Attention Deficit Hyperactivity Disorder (ADHD) [Weyandt, Swentosky and Gudmundsdottir (2013)], and Schizophrenia [Niznikiewicz, Kubicki and Shenton (2003)].

Traditional multimodal analyses of rs-fMRI and DTI data have largely focused on post-hoc statistical compar-

*Corresponding author
Email address: Shimona.Niharika.Dsouza@jhu.edu
(N.S. D'Souza)

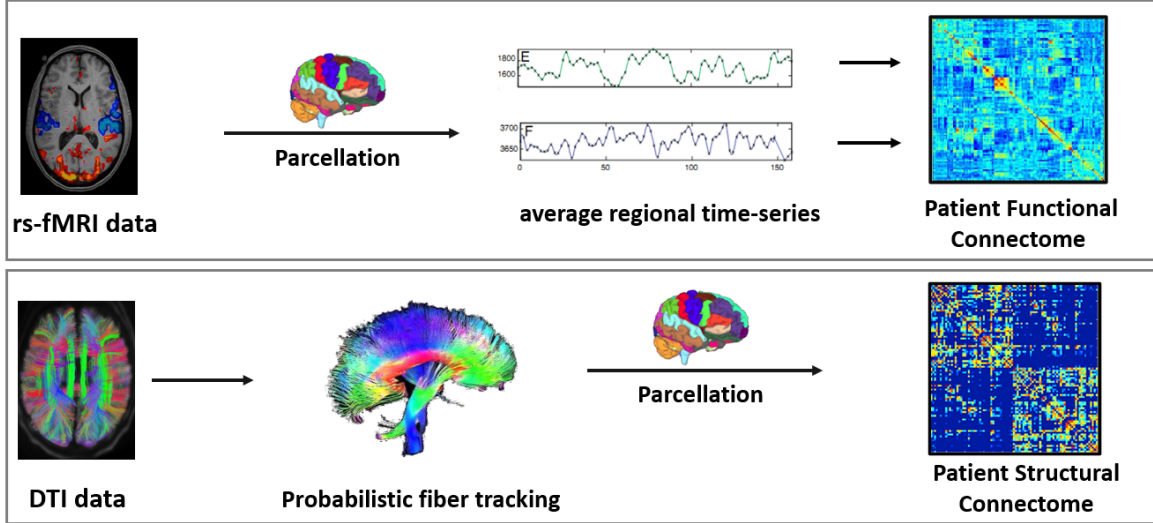


Figure 1: **Top:** For the fMRI data, we group voxels in the brain into ROIs defined by a standard atlas and compute the average time courses for each ROI. The correlation matrix captures the synchrony in the average time courses. **Bottom** Tractography is performed on the raw DWI data to track the path of neuronal fibers in the brain. Based on the parcellation scheme, we construct a map of the fibre tracts between ROIs in the brain. The same parcellation scheme is used for both modalities.

isons of features extracted from the data. For example, simple statistical differences in rs-fMRI and DTI connectivity between subjects have been used to discover disrupted patterns of brain organization in Alzheimer’s disease [Hahn, Myers, Prigarin, Rodenacker, Kurz, Förstl, Zimmer, Wohlschläger and Sorg (2013)] and Progressive Supranuclear Palsy (PSP) [Whitwell, Avula, Master, Vemuri, Senjem, Jones, Jack Jr and Josephs (2011)]. On a population level, classical multivariate analysis [Goble, Coxon, Van Impe, Geurts, Van Hecke, Sunaert, Wenderoth and Swinnen (2012) Andrews-Hanna, Snyder, Vincent, Lustig, Head, Raichle and Buckner (2007)] or random effects models [Propper, ODonnell, Whalen, Tie, Norton, Suarez, Zollei, Radmanesh and Golby (2010)] are employed to independently compute and then combine features from both modalities. Despite their past success at biomarker discovery, these techniques often fail to generalize at a patient-specific level. Furthermore, they often ignore higher-order interactions between multiple subsystems in the brain, which is known to be critical for understanding complex neuropsychiatric disorders [Kaiser, Hudac, Shultz, Lee, Cheung, Berken, Deen, Pitskel, Sugrue, Voos et al. (2010); Koshino, Carpenter, Minshew, Cherkassky, Keller and Just (2005)]. These shortcomings have paved the way for the development of the network based view of brain connectivity that simultaneously accounts for both inter-subject and intra-subject variability.

In the case of fMRI, network-based models often group voxels in the brain into regions of interest (ROIs) using a standard anatomical or functional atlas. Next, the functional relationships between these regions are determined based on the synchrony between representative (often average) regional time series. This information is typically represented in terms of a static functional connectivity ma-

trix as shown in Fig. 1 (top). In case of DTI, tractography is used to estimate the fiber tracts between the ROIs in the brain from the voxel-level diffusion tensors, from which features such as the anisotropy or the number of fibers can be extracted. Similar to the functional connectome, the structural connectivity matrix captures the strength of the pairwise anatomical connection between different ROIs, as seen in Fig. 1 (bottom).

Some of the simplest approaches to analyzing network properties borrow heavily from the field of graph theory. For example, the works of [Bullmore and Sporns (2009); Rubinov and Sporns (2010); Sporns, Chialvo, Kaiser and Hilgetag (2004)] use aggregate network measures, such as node degree, betweenness centrality, and eigenvector centrality to study the organization of the brain. These measures compactly summarize the connectivity information onto a restricted set of nodes that can be mapped back to the brain. A more global network property is small-worldedness [Bassett and Bullmore (2006)], which describes an architecture of sparsely connected clusters of nodes. Complementary changes in small-worldedness in both anatomical and functional networks have been well documented across the literature [Park, Kim, Kim and Kim (2008); Sun, Yin, Fang, Yan, Wang, Bezerianos, Tang, Miao and Sun (2014)], with concurrent disruptions of functional networks [Wang, Kalmar, He, Jackowski, Chepenik, Edmiston, Tie, Gong, Shah, Jones et al. (2009)] or structural networks [Wang, Su, Zhou, Chou, Chen, Jiang and Lin (2012)] implicated in neuropsychiatric disorders such as schizophrenia. The main limitation of these approaches is that they independently analyze the fMRI and DTI data, and as such, draw heuristic conclusions about the relationship between the two modalities.

Community detection techniques have been widely used

for understanding the organization of complex systems such as the brain [Bardella, Bifone, Gabrielli, Gozzi and Squartini (2016)]. Other examples include the work of [Venkataraman, Kubicki and Golland (2013)] that identifies abnormal connectivity in schizophrenia, and [Venkataraman, Yang, Pelphrey and Duncan (2016)], which characterizes the social and communicative deficits associated with autism. An alternative network topology is the hub-spoke model, used by [Venkataraman et al. (2013), Venkataraman, Kubicki and Golland (2012), Venkataraman, Duncan, Yang and Pelphrey (2015)], that targets regions associated with a large number of altered rs-fMRI connections. These methods, however, exclusively focus on functional connectivity and do not incorporate structure. In this light, the work of [Venkataraman, Rathi, Kubicki, Westin and Golland (2011)] proposes a probabilistic framework that jointly models latent anatomical and functional connectivity to discover population-level differences in schizophrenia. Similarly, the work of [Higgins, Kundu and Guo (2018)] uses a unified Bayesian framework to identify gender-differences in multimodal connectivity patterns across different age groups. While successful at combining multi-modal information for group differentiation, these techniques do not directly address inter-individual variability.

Data-driven methods integrating structural and functional connectivity focus heavily on groupwise discrimination from the static connectomes. These methods usually follow a two-step approach where feature selectors and discriminators are trained sequentially in a pipeline. For example, the authors in [Wee, Yap, Zhang, Denny, Browndyke, Potter, Welsh-Bohmer, Wang and Shen (2012)] combine graph theoretic features computed from rs-fMRI and DTI graphs with Support Vector Machines (SVMs) to identify individuals with Mild Cognitive Impairment. Another example is the work of [Sui, He, Yu, Rogers, Pearlson, Mayer, Bustillo, Canive, Calhoun et al. (2013)], which employs a pipeline consisting of joint-Independent Component Analysis (j-ICA) on the two modalities followed by Canonical Correlation Analysis (CCA) to combine them and distinguish schizophrenia patients from controls. In contrast to the pipelined approaches, end-to-end deep learning methods combining feature selection and prediction are becoming ubiquitous in neuroimaging studies. These are highly successful due to their ability to learn complex abstractions directly from input data. As an example, the work of [Aghdam, Sharifi and Pedram (2018)] uses a Deep Belief Network (DBN) on multimodal data to disambiguate patients with Autism Spectrum Disorder from healthy controls. However, none of the above methods tackle continuous-valued prediction, for example, quantifying a continuous level of deficit.

In the continuous prediction realm, the authors of [Kawahara, Brown, Miller, Booth, Chau, Grunau, Zwicker and Hamarneh (2017)] developed an end-to-end convolutional neural network to predict cognitive outcomes from DTI connectomes. On the other hand, the authors of

DSouza, Nebel, Wymbs, Mostofsky and Venkataraman (2019b) combine dictionary learning on the rs-fMRI correlations with an Artificial Neural Network (ANN) to predict clinical severity in ASD patients. While promising, these methods focus on a single neuroimaging modality and do not exploit complementary interactions between structural and functional connectivity.

There is now growing evidence that functional connectivity is a dynamic process that toggles between different intrinsic states evolving over a static structural connectome [Cabral, Kringelbach and Deco (2017)]. These states manifest over short time windows that are typically of the order of a tens of seconds to a few minutes. Several studies such as [Price, Wee, Gao and Shen (2014); Rashid, Damaraju, Pearlson and Calhoun (2014)] indicate the importance of modeling this evolution for characterizing neuropsychiatric disorders such as schizophrenia and Autism Spectrum Disorder (ASD). The dynamic connectivity among ROIs in the brain is typically captured via a sliding window protocol, defined by the window length and stride, as illustrated in Fig. 2. The window length defines the length of the time sequence considered by each dynamic correlation matrix, while the stride controls the overlap in successive sliding windows. Recently, model based alternatives that detect dynamic changes in correlation between large-scale brain networks such as the Default Mode Network, Somatosensory Network etc have been developed. An example is the Dynamic Conditional Correlation (DCC) protocol that was initially developed in the econometrics and finance literature [Engle (2002)] and later adapted to the study of brain organization using rs-fMRI [Lindquist (2016)]. It poses a time-varying matrix estimation problem to explicitly model the evolution of connectivity patterns in the brain, and has shown robustness in the test-retest setting [Lindquist, Xu, Nebel and Caffo (2014)] with rs-fMRI. Unfortunately, this method is unstable when scaled up [Aielli (2013); Caporin and McAleer (2013)], for example to a whole brain ROI-level analysis of dynamic connectivity, likely due to ill conditioning of the correlation matrices in the absence of additional regularization. Consequently, most dynamic connectivity studies continue to rely on sliding-window correlations as inputs. Examples include [Cai, Zille, Stephen, Wilson, Calhoun and Wang (2017)], where the authors use a sparse decomposition of the rs-fMRI connectomes, or [Rabany, Brocke, Calhoun, Pittman, Corbera, Wexler, Bell, Pelphrey, Pearlson and Assaf (2019)], which employs a temporal clustering for ASD/control discrimination. Nevertheless, these approaches focus exclusively on rs-fMRI and completely ignore structural information.

We propose a deep-generative hybrid model, i.e. the deep sr-DDL, that integrates structural and dynamic functional connectivity with behavior into a unified optimization framework. Our deep sr-DDL framework has two main components, (1) a generative dictionary learning component to represent the multimodal data and (2) a deep network to predict behavioral scores. Our generative

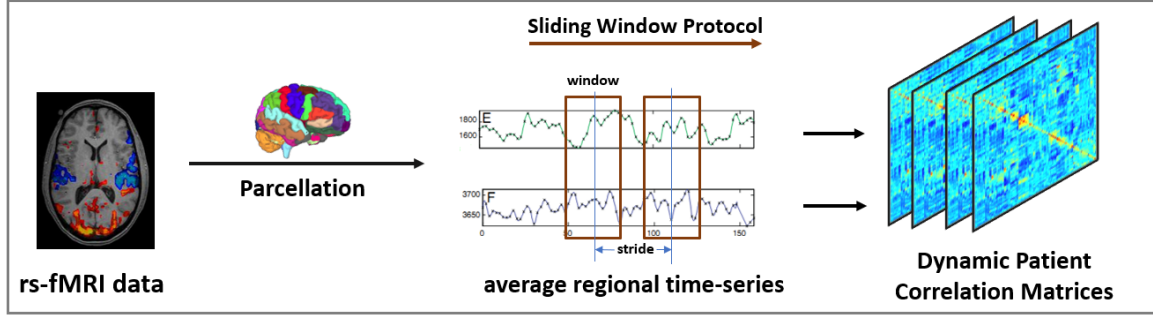


Figure 2: First, the ROI’s defined by a standard atlas are used to compute regional time series. Then, a sliding window protocol defined by window length and stride is applied to extract the dynamic patient correlation matrices. As in the static case, the dynamic matrices measure the synchrony between regional time series, but as a function of time.

component is a structurally regularized Dynamic Dictionary Learning (sr-DDL), which uses a DTI tractography prior to regularize a matrix factorization of the dynamic rs-fMRI correlation matrices. Specifically, we decompose dynamic rs-fMRI correlation matrices into a collection of shared bases, and time-varying subject specific loadings, similar to the static setup introduced in [Eavani, Satterthwaite, Filipovich, Gur, Gur and Davatzikos (2015)] and extended by [D’Souza, Nebel, Wymbs, Mostofsky and Venkataraman (2018); DSouza, Nebel, Wymbs, Mostofsky and Venkataraman (2019a); DSouza et al. (2019b)]. Simultaneously, these loadings are input to a deep network which is comprised of a Long-Short Term Memory (LSTM) module to model temporal trends and an ANN that predicts clinical scores. Our end-to-end optimization procedure jointly estimates the bases, loadings, and neural network weights most predictive of the clinical profile, as opposed to a modular, pipelined approach.

A preliminary version of our work will appear in MICCAI 2020, and is currently available on Arxiv [D’Souza, Nebel, Crocetti, Wymbs, Robinson, Mostofsky and Venkataraman (2020)]. Here, we provide a detailed analysis of our framework where we validate on two separate real-world datasets. The first of these includes a subset of healthy adults from the publicly available Human Connectome Project (HCP) [Van Essen, Ugurbil, Auerbach, Barch, Behrens, Bucholz, Chang, Chen, Corbetta, Curtiss et al. (2012)]. This helps us evaluate the efficacy of our framework at predicting cognitive outcomes from the rs-fMRI and DTI scans. Next, we examine a clinical dataset consisting of children diagnosed with Autism Spectrum Disorder (ASD). The presentation of ASD is known to be heterogeneous with individuals exhibiting a wide spectrum of behavioral impairments in terms of social reciprocity, communicative functioning, and repetitive/restrictive behaviours [Spitzer and Williams (1980)], quantified via clinical severity measures. We observed that our method outperforms several state-of-the-art approaches at predicting behavioral performance in unseen individuals from their connectomics data for both datasets. In summary, our joint objective balances generalizability

with interpretability, bridging the representational gap between structure, function and behavior. Our experiments highlight the potential of our deep sr-DDL framework for providing a more holistic view of neuropsychiatric diseases.

2. Materials and Methods

2.1. A Deep Generative Hybrid Model to integrate Multimodal and Dynamic Connectivity with Behavior

Fig. 3 presents a graphical overview of our framework. We have three sets of inputs to the model for each individual namely, the dynamic individual-specific correlation matrices, the DTI structural connectome graph (upper left), and the set of scalar clinical scores (bottom right). We use the sliding window approach in Fig. 2 to extract dynamic rs-fMRI correlation matrices and tractography to extract the DTI connectomes as shown in Fig. 1. The DTI input to our model is the Graph Laplacian obtained from a binary DTI adjacency matrix capturing the presence/absence of a fiber between regions. Finally, the behavioral scores for each individual are obtained from an expert assessment. This score can correspond to either cognitive outcomes or severity of symptoms in case of neurodevelopmental diseases.

The green box in Fig. 3 describes the generative component of our framework. Here, the dynamic rs-fMRI correlation matrices are decomposed using a structurally regularized dynamic dictionary learning (sr-DDL). The columns in the bases subnetworks capture representative patterns common to the cohort. The loading coefficients differ across subjects, and evolve over time. At each time-point/observation, they determine the contribution of each basis to the dynamic functional connectivity profile of the individual. Finally, the DTI Graph Laplacians re-weight the decomposition to focus on the functional connectivity between anatomically linked regions. The gray box denotes the deep networks part of our model. This network combines a Long Short Term Memory (LSTM) module with an Artificial Neural Network (ANN) to predict multiple behavioral scores. The LSTM models the temporal trends in the subject-specific loading coefficients giving rise

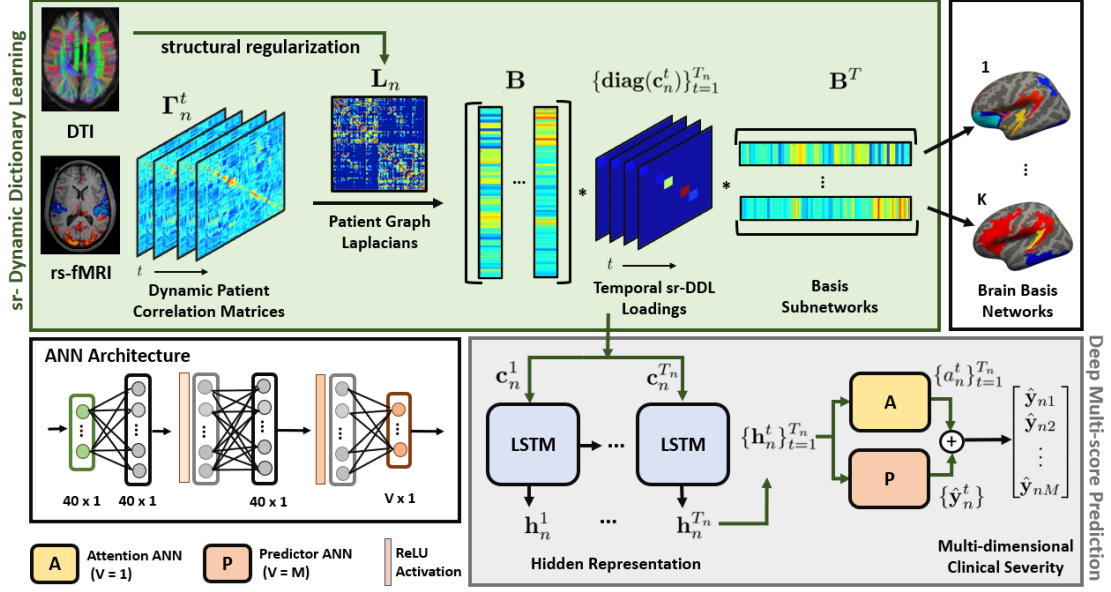


Figure 3: Framework to integrate structural and dynamic functional connectivity for clinical severity prediction **Green Box**: The generative sr-DDL module. The rs-fMRI dynamic correlation matrices are decomposed into the subnetwork basis and time-varying subject-specific loadings. The DTI connectivity regularizes this decomposition. **Gray Box**: Deep LSTM-ANN module for multi-score prediction. The sr-DDL coefficients are input into the LSTM to generate a hidden representation. The predictor ANN (P-ANN) generates a time varying estimate for the scores, while the attention ANN (A-ANN) weights the predictions across time to generate the final clinical severity estimate.

to a hidden representation. The ANN then uses this representation to predict the corresponding behavioral outcomes.

Dynamic Dictionary Learning for rs-fMRI data.

We denote the set of time varying functional correlation matrices for individual n by the set $\{\Gamma_n^t\}_{t=1}^{T_n} \in \mathcal{R}^{P \times P}$. Here, T_n denotes the number of sliding windows applied to the rs-fMRI scan, and P is the number of ROIs in the parcellation scheme. As seen in Fig. 3 (green box), we model this information using a group average basis, and subject-specific temporal loadings. The dictionary $\mathbf{B} \in \mathcal{R}^{P \times K}$ is a concatenation of K elemental bases vectors $\mathbf{b}_k \in \mathcal{R}^{P \times 1}$, i.e. $\mathbf{B} := [\mathbf{b}_1 \ \mathbf{b}_2 \ \dots \ \mathbf{b}_K]$, where $K \ll P$. This basis captures representative brain states which each subject cycles through over the course of the scan. We further constrain the basis vectors to be orthogonal to each other. This constraint acts as an implicit regularizer, ensuring that the learned subnetworks are uncorrelated, yet explain the rs-fMRI data well. While the bases are shared across the cohort, the strength of their combination differs across individuals and varies over time. These loadings are denoted by the set $\{\mathbf{c}_n^t\}_{t=1}^{T_n}$ and combine the basis subnetworks uniquely to best explain each subject's functional connectivity. We introduce an explicit non-negativity constraint \mathbf{c}_{nk}^t to ensure that the positive semi-definiteness of Γ_n^t is preserved. The complete rs-fMRI data representation takes the following form:

$$\Gamma_n^t \approx \sum_k \mathbf{c}_{nk}^t \mathbf{b}_k \mathbf{b}_k^T \quad s.t. \quad \mathbf{c}_{nk} \geq 0, \quad \mathbf{B}^T \mathbf{B} = \mathcal{I}_K, \quad (1)$$

where \mathcal{I}_K is the $K \times K$ identity matrix. As seen in Eq. (1), the subject-specific loading vector at time t , $\mathbf{c}_n^t := [\mathbf{c}_{n1}^t \ \dots \ \mathbf{c}_{nK}^t]^T \in \mathcal{R}^{K \times 1}$ models the heterogeneity in the cohort. Denoting $\text{diag}(\mathbf{c}_n^t)$ as a diagonal matrix with the K subject-specific coefficients on the diagonal and off-diagonal terms set to zero, Eq. (1) can be re-written in the following matrix form:

$$\Gamma_n^t \approx \mathbf{B} \text{diag}(\mathbf{c}_n^t) \mathbf{B}^T \quad s.t. \quad \mathbf{c}_{nk}^t \geq 0, \quad \mathbf{B}^T \mathbf{B} = \mathcal{I}_K \quad (2)$$

Finally, this matrix factorization serves to reduce the dimensionality of the rs-fMRI data, while simultaneously modeling group-level and subject-specific information.

Structural Regularization from DTI data. We denote the structural connectome graph for individual n by $\mathcal{G}_n(\mathcal{V}, \mathcal{E}, \mathbf{A}_n)$. Here \mathcal{V} are the vertices defined on the P ROIs, \mathcal{E} are the graph edges defined by the binary adjacency matrix $\mathbf{A}_n \in \mathcal{R}^{P \times P}$. We compute the corresponding Normalized Graph Laplacian [Banerjee and Jost (2008)] as $\mathbf{L}_n = \mathbf{V}_n^{-\frac{1}{2}} (\mathbf{V}_n - \mathbf{A}_n) \mathbf{V}_n^{-\frac{1}{2}}$, where $\mathbf{V}_n = \text{diag}(\mathbf{A}_n \mathbf{1})$ is the degree matrix and $\mathbf{1}$ is the vector of all ones. In the past, the spectral properties of the Graph Laplacian have made it a popular choice as a spatial regularizer in computer vision [Liu, Liang, Zhou, He, Hao, Song, Yu, Liu, Liu and Jiang (2008)], genetics [Feng, Gao, Liu, Zheng and Yu (2017)] and neuroimaging [Atasoy et al. (2016); Cuingnet, Glaunès, Chupin, Benali and Colliot (2012)]. We extend this concept to regularizing our functional matrix decomposition by substituting the ℓ_2 penalty in Eq. (2) using the Weighted Frobenius Norm $\|\cdot\|_{\mathbf{L}_n}$ [Manton, Mahony and Hua (2003); Schnabel and Toint (1983)]. Mathematically,

given this structural regularization, the approximation error of Eq. (2) takes the following form:

$$\|\Gamma_n^t - \mathbf{B} \text{diag}(\mathbf{c}_n^t) \mathbf{B}^T\|_{\mathbf{L}_n} = \text{Tr} \left[(\Gamma_n^t - \mathbf{B} \text{diag}(\mathbf{c}_n^t) \mathbf{B}^T) \mathbf{L}_n (\Gamma_n^t - \mathbf{B} \text{diag}(\mathbf{c}_n^t) \mathbf{B}^T) \right] \quad (3)$$

Here, $\text{Tr}[\mathbf{M}]$ is the trace operator, which sums the diagonal elements of the argument matrix \mathbf{M} . Essentially, the matrix \mathbf{L}_n refocuses the factorization such that region pairs with an underlying anatomical connection have a greater contribution to the approximation error than region pairs without an anatomical connection. Based on the formulation in Eq. (3), the final sr-DDL objective $\mathcal{D}(\cdot)$ can be expressed as follows:

$$\mathcal{D}(\mathbf{B}, \{\mathbf{c}_n^t\}; \{\Gamma_n^t\}, \mathbf{L}_n) = \sum_t \frac{1}{T_n} \|\Gamma_n^t - \mathbf{B} \text{diag}(\mathbf{c}_n^t) \mathbf{B}^T\|_{\mathbf{L}_n} \quad s.t. \quad \mathbf{c}_{nk}^t \geq 0, \quad \mathbf{B}^T \mathbf{B} = \mathcal{I}_K \quad (4)$$

Deep Multiscore Prediction. As seen in the gray box in Fig. 3, the subject-specific coefficients $\{\mathbf{c}_n^t\}$ are input to an LSTM-ANN to predict the clinical scores, as parametrized by the weights Θ . The M clinical scores for each individual are concatenated into a vector $\mathbf{y}_n := [\mathbf{y}_{n1} \dots \mathbf{y}_{nM}]^T \in \mathcal{R}^{M \times 1}$. The LSTM models the temporal variations in the coefficients $\{\mathbf{c}_n^t\}$ to generate a hidden representation $\{\mathbf{h}_n^t\}_{t=1}^{T_n}$. From here, the Predictor ANN (P-ANN) generates a time varying estimates of the scores $\{\hat{\mathbf{y}}_n^t\}_{t=1}^{T_n} \in \mathcal{R}^{M \times 1}$. At the same time, the Attention ANN (A-ANN) generates T_n scalars from the hidden representation. These are then softmax across time to obtain the attention weights: $\{a_n^t\}_{t=1}^{T_n}$. The final prediction is an attention-weighted average across the time estimates, which takes the following form:

$$\hat{\mathbf{y}}_n = \sum_t \hat{\mathbf{y}}_n^t a_n^t \quad (5)$$

Effectively, the attention weights determine which time points for each subject are most relevant for behavioral prediction. Additionally, they allow us to handle rs-fMRI scans of varying durations. Mathematically, we compute the multi-score prediction error $\mathcal{L}(\cdot)$ using the Mean Squared Error (MSE) loss function as follows:

$$\mathcal{L}(\{\mathbf{c}_n^t\}, \mathbf{y}_n; \Theta) = \|\hat{\mathbf{y}}_n - \mathbf{y}_n\|_F^2 = \left\| \sum_{t=1}^{T_n} \hat{\mathbf{y}}_n^t a_n^t - \mathbf{y}_n \right\|_F^2 \quad (6)$$

At a high level, the deep network distills the temporal information to best predict each subject's clinical profile.

Joint Objective for Multimodal Integration. We combine the complementary viewpoints in Eq. (4) and

Eq. (6) into a single joint objective below:

$$\begin{aligned} \mathcal{J}(\mathbf{B}, \{\mathbf{c}_n^t\}, \Theta; \{\Gamma_n^t\}, \mathbf{L}_n, \{\mathbf{y}_n\}) \\ = \underbrace{\sum_n \mathcal{D}(\mathbf{B}, \{\mathbf{c}_n^t\}; \{\Gamma_n^t\}, \mathbf{L}_n)}_{\text{sr-DDL loss}} + \lambda \underbrace{\sum_n \mathcal{L}(\Theta, \{\mathbf{c}_n^t\}; \mathbf{y}_n)}_{\text{deep network loss}} \\ = \sum_n \sum_t \frac{1}{T_n} \|\Gamma_n^t - \mathbf{B} \text{diag}(\mathbf{c}_n^t) \mathbf{B}^T\|_{\mathbf{L}_n} \\ + \lambda \sum_n \mathcal{L}(\Theta, \{\mathbf{c}_n^t\}; \mathbf{y}_n) \quad s.t. \quad \mathbf{c}_{nk}^t \geq 0, \quad \mathbf{B}^T \mathbf{B} = \mathcal{I}_K \quad (7) \end{aligned}$$

Here, λ is a hyperparameter than balances the tradeoff between the representation loss $\mathcal{D}(\cdot)$ and the prediction loss $\mathcal{L}(\cdot)$. $\{\mathbf{B}, \{\mathbf{c}_n^t\}, \Theta\}$ are the variables to optimize.

Architectural Details. Our proposed ANN architecture is highlighted in the white box to the bottom left of Fig. 3. Our modeling choices carefully control for representational capacity and convergence of our coupled optimization procedure. Since the input to the network, i.e. the coefficient vector \mathbf{c}_n^t is essentially low dimensional, we opt for a two layered LSTM with the hidden layer width as 40. Both the P-ANN and the A-ANN are fully connected neural networks with two hidden layers of width 40. Since the A-ANN outputs a scalar, the width of its output layer is one, while that of the P-ANN is of size M , i.e. the number of behavioral scores. We use a Rectified Linear Unit (ReLU) as the activation function for each hidden layer, as we found that this choice is robust to issues with vanishing gradients and saturation that commonly confound the training of deep neural networks [Glorot, Bordes and Bengio (2011)].

2.2. Coupled Optimization Strategy

We employ the alternating minimization technique in order to infer the set of hidden variables $\{\mathbf{B}, \{\mathbf{c}_n^t\}, \Theta\}$. Namely, we optimize Eq. (7) for each output variable, while holding the other unknowns constant.

We utilize the fact that there is a closed-form Procrustes solution for quadratic objectives of the form $\|\mathbf{M} - \mathbf{B}\|_F^2$ [Everson (1998)]. However, Eq. (7) is bi-quadratic in \mathbf{B} , so it cannot be directly applied. Therefore, we adopt the strategy in [DSouza, Nebel, Wymbs, Mostofsky and Venkataraman (2020); DSouza et al. (2019a,b)] of introducing $\sum_n T_n$ constraints of the form $\mathbf{D}_n^t = \mathbf{B} \text{diag}(\mathbf{c}_n^t)$. These constraints are enforced via the Augmented Lagrangian algorithm with corresponding constraint variables $\{\Lambda_n^t\}$. Thus, our objective from Eq. (7)

now becomes:

$$\begin{aligned} \mathcal{J}_c = & \sum_{n,t} \frac{1}{T_n} \|\Gamma_n^t - \mathbf{D}_n^t \mathbf{B}^T\|_{\mathbf{L}_n} + \lambda \sum_n \mathcal{L}(\Theta, \{\mathbf{c}_n^t\}; \mathbf{y}_n) \\ & + \sum_{n,t} \frac{\gamma}{T_n} \left[\text{Tr} [(\Lambda_n^t)^T (\mathbf{D}_n^t - \mathbf{B} \text{diag}(\mathbf{c}_n^t))] \right] \\ & + \sum_{n,t} \frac{\gamma}{T_n} \left[\frac{1}{2} \|\mathbf{D}_n^t - \mathbf{B} \text{diag}(\mathbf{c}_n^t)\|_F^2 \right] \\ \text{s.t. } & \mathbf{c}_{nk}^t \geq 0, \mathbf{B}^T \mathbf{B} = \mathcal{I}_K \end{aligned} \quad (8)$$

The Frobenius norm terms $\|\mathbf{D}_n^t - \mathbf{B} \text{diag}(\mathbf{c}_n^t)\|_F^2$ regularize the trace constraints during the optimization. Observe that Eq. (8) is convex in the set $\{\mathbf{D}_n^t\}$, which allows us to optimize this variable via standard procedures. The constraint parameter is fixed at $\gamma = 20$, based on the guidelines in the literature [Nocedal and Wright (2006)].

Fig. 4 depicts our alternating minimization strategy. We describe each individual block in detail below:

Step 1: Closed form solution for \mathbf{B} . Notice that Eq. (8) reduces to the following quadratic form in \mathbf{B} :

$$\mathbf{B}^* = \arg \min_{\mathbf{B}: \mathbf{B}^T \mathbf{B} = \mathcal{I}_K} \|\mathbf{M} - \mathbf{B}\|_F^2 \quad (9)$$

where \mathbf{M} is computed as:

$$\begin{aligned} \mathbf{M} = & \sum_n \frac{1}{T_n} \sum_t (\Gamma_n^t \mathbf{L}_n + \mathbf{L}_n \Gamma_n^t) \mathbf{D}_n^t + \\ & \sum_n \frac{1}{T_n} \left[\sum_t \frac{\gamma}{2} \mathbf{D}_n^t \text{diag}(\mathbf{c}_n^t) + \gamma \Lambda_n^t \text{diag}(\mathbf{c}_n^t) \right] \end{aligned} \quad (10)$$

We know that \mathbf{B} has a closed-form Procrustes solution [Everson (1998)] computed as follows. Given the singular value decomposition $\mathbf{M} = \mathbf{U} \mathbf{S} \mathbf{V}^T$, we have:

$$\mathbf{B}^* = \mathbf{U} \mathbf{V}^T$$

In essence, \mathbf{B} spans the anatomically weighted space of subject-specific dynamic correlation matrices.

Step 2: Updating the sr-DDL loadings $\{\mathbf{c}_n^t\}$. The objective \mathcal{J}_c in Eq. (8) decouples across subjects. We can also incorporate the non-negativity constraint $\mathbf{c}_{nk}^t \geq 0$ by

passing an intermediate vector $\hat{\mathbf{c}}_n^t$ through a ReLU. Thus:

$$\mathbf{c}_n^t = \text{ReLU}(\hat{\mathbf{c}}_n^t) \quad (11)$$

The ReLU pre-filtering allows us to optimize an unconstrained version of Eq. (8), as follows:

$$\begin{aligned} \mathcal{J}_{\hat{c}} = & \lambda \sum_n \mathcal{L}(\Theta, \{\mathbf{c}_n^t\}; \mathbf{y}_n) \\ & + \sum_{n,t} \frac{\gamma}{T_n} \left[\text{Tr} [(\Lambda_n^t)^T (\mathbf{D}_n^t - \mathbf{B} \text{diag}(\mathbf{c}_n^t))] \right] \\ & + \sum_{n,t} \frac{\gamma}{T_n} \left[\frac{1}{2} \|\mathbf{D}_n^t - \mathbf{B} \text{diag}(\mathbf{c}_n^t)\|_F^2 \right] \end{aligned} \quad (12)$$

This optimization can be performed via the stochastic ADAM algorithm [Kingma and Ba (2015)] by backpropagating the gradients from the loss in Eq. (12) upto the input $\{\hat{\mathbf{c}}^t\}$. Experimentally, we set the initial learning rate to be 0.01, scaled by 0.9 per 10 iterations. Essentially, this optimization couples the parametric gradient from the Augmented Lagrangian formulation with the backpropagated gradient from the deep network (parametrized by fixed Θ). After convergence, the thresholded loadings $\mathbf{c}_n^t = \text{ReLU}(\hat{\mathbf{c}}_n^t)$ are used in the subsequent steps of the minimization.

Step 3: Updating the Deep Network weights- Θ . We use backpropagation on the loss $\mathcal{L}(\cdot)$ to solve for the unknowns Θ . Notice that we can handle missing clinical data by dropping the contributions of the unknown value of \mathbf{y}_{nm} to the network loss during backpropagation. Again, we use the ADAM optimizer [Kingma and Ba (2015)] with random initialization at the first main iteration of alternating minimization. We employ a learning rate of 10^{-4} , scaled by 0.95 every 5 epochs, and batch-size 1. Additionally, we train the network only for 50 epochs to avoid overfitting.

Step 4: Updating the Constraint Variables $\{\mathbf{D}_n^t, \Lambda_n^t\}$. Each of the primal variables $\{\mathbf{D}_n^t\}$ has a closed form solution given by:

$$[\mathbf{D}_n^t]^k = \mathbf{K} \mathbf{F} \quad (13)$$

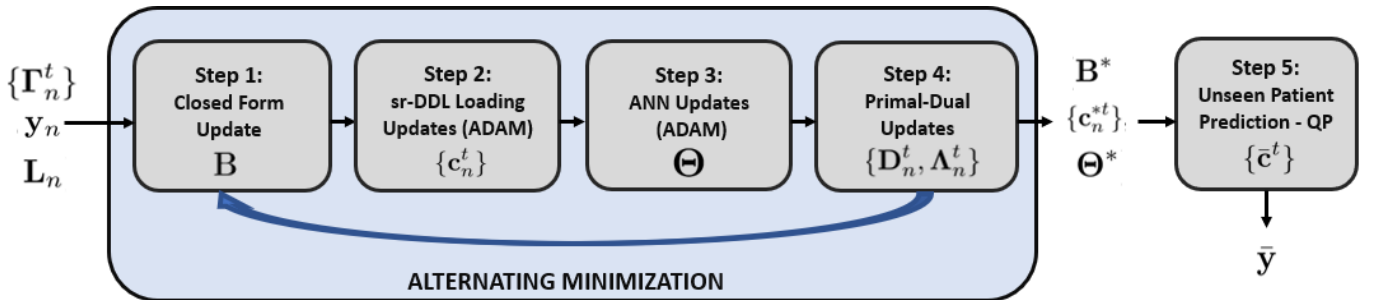


Figure 4: Alternating minimization strategy for joint optimization of Eq. (8)

where, $\mathbf{K} = (\text{diag}(\mathbf{c}_n)\mathbf{B}^T + \mathbf{\Gamma}_n^t \mathbf{L}_n \mathbf{B} + \mathbf{L}_n \mathbf{\Gamma}_n^t \mathbf{B} - \gamma \mathbf{\Lambda}_n)$ and $\mathbf{F} = (\gamma \mathcal{I}_K + 2\mathbf{L}_n)^{-1}$. We update the dual variables $\{\mathbf{\Lambda}_n\}$ via gradient ascent:

$$[\mathbf{\Lambda}_n^t]^{k+1} = [\mathbf{\Lambda}_n^t]^k + \eta_k([\mathbf{D}_n^t]^k - \mathbf{B}\text{diag}(\mathbf{c}_n)) \quad (14)$$

We cycle through the primal-dual updates for $\{\mathbf{D}_n^t\}$ and $\{\mathbf{\Lambda}_n^t\}$ in Eq. (13-14) to ensure that the constraints $\mathbf{D}_n^t = \mathbf{B}\text{diag}(\mathbf{c}_n^t)$ are satisfied with increasing certainty at each iteration. The learning rate parameter η_k for the gradient ascent step is selected to guarantee sufficient decrease in the objective for every iteration of alternating minimization. In practice, we initialize η_0 to 10^{-3} , and scale it by 0.75 at each iteration k .

Step 5: Prediction on Unseen Data. In our cross-validated setting, we must compute the sr-DDL loadings $\{\bar{\mathbf{c}}^t\}_{t=1}^T$ for a new subject based on the \mathbf{B}^* obtained from the training procedure and the new rs-fMRI correlation matrices $\{\bar{\mathbf{\Gamma}}^t\}$ and DTI Laplacians $\bar{\mathbf{L}}$. As we do not know the score $\bar{\mathbf{y}}$ for this individual, we need remove the contribution $\mathcal{L}(\cdot)$ from Eq. (8) and assume that the constraints $\bar{\mathbf{D}}^t = \mathbf{B}^* \text{diag}(\bar{\mathbf{c}}^t)$ are satisfied with equality. This effectively eliminates the Lagrangian terms. Essentially, the optimization for $\{\bar{\mathbf{c}}^t\}$ now reduces to \bar{T}_n decoupled quadratic programming (QP) objectives \mathcal{Q}_t :

$$\begin{aligned} \bar{\mathbf{c}}^{*t} &= \arg \min_{\bar{\mathbf{c}}^t} \frac{1}{2} (\bar{\mathbf{c}}^t)^T \bar{\mathbf{H}} \bar{\mathbf{c}}^t + \bar{\mathbf{f}}^T \bar{\mathbf{c}}^t \quad s.t. \quad \bar{\mathbf{A}} \bar{\mathbf{c}}^t \leq \bar{\mathbf{b}} \\ \bar{\mathbf{H}} &= 2(\mathbf{B}^{*T} \bar{\mathbf{L}} \mathbf{B}^*); \\ \bar{\mathbf{f}} &= -[\mathcal{I}_K \circ (\mathbf{B}^{*T} (\bar{\mathbf{\Gamma}}^t \bar{\mathbf{L}} + \bar{\mathbf{L}} \bar{\mathbf{\Gamma}}^t) \mathbf{B}^*)] \mathbf{1}; \\ \bar{\mathbf{A}} &= -\mathcal{I}_K \quad \bar{\mathbf{b}} = \mathbf{0} \end{aligned} \quad (15)$$

Where \circ is the elementwise Hadamard product. Notice that decoupling the objective across time allows us to parallelize this computation. Additionally, since $\bar{\mathbf{H}}$ is positive semi-definite, the formulation in Eq. (15) is convex, leading to an efficient QP solution. Finally, we estimate $\bar{\mathbf{y}}$ via a forward pass through the LSTM-ANN.

2.2.1. Implementation Details

Parameter Settings. Our deep-generative hybrid has two free parameters: namely the penalty λ , which con-

trols the tradeoff between data representation and clinical prediction, and K , the number of networks. For our experiments, we chose $K = 15$ for both datasets based on the knee point of the eigenspectrum of the correlation matrices $\mathbf{\Gamma}_n^t$ (see Fig. 5). The tradeoff parameter is set to $\lambda = 3$ for both datasets, as we empirically found that this choice gives a good performance on the test data without overfitting during training. We discuss the sensitivity to this parameter in Section 4.1.

Initialization. Our coupled optimization strategy requires us to initialize the basis \mathbf{B} , coefficients $\{\mathbf{c}_n^t\}$, the deep network weights $\mathbf{\Theta}$ and the constraint variable pairs $\{\mathbf{D}_n^t, \mathbf{\Lambda}_n^t\}$. We randomly initialize the deep network weights at the first main iteration. We employ a soft-initialization for $\{\mathbf{B}, \{\mathbf{c}_n^t\}\}$ by solving the dictionary objective in Eq. (4) without the LSTM-ANN loss terms for 20 iterations. We then initialize $\mathbf{D}_n^t = \mathbf{B}\text{diag}(\mathbf{c}_n^t)$ and $\mathbf{\Lambda}_n^t = \mathbf{0}$ which lie in the feasible set for our constraints. We empirically observed that this soft initialization helps stabilize the optimization to provide improved predictive performance in fewer main iterations when compared with a completely random initialization.

Finally, the meta-data and code used in this study are available on a public repository hosted on Github¹.

2.3. Baseline Comparison Techniques

We evaluate the performance of our framework against three different classes of baselines, each highlighting the benefit of specific modeling choices made by our method.

(15) Our first baseline class is a two stage configuration as illustrated in Fig. 6 that combines feature extraction on the dynamic rs-fMRI and DTI data, with a deep learning predictor. These feature engineering techniques are drawn from a set of well established statistical (Independent Component Analysis in Subsection 2.3.2) and graph theoretic techniques (Betweenness Centrality in Subsection 2.3.1), known to provide rich feature representations. The learned features are then input to the same deep LSTM-ANN network used by our method. This network is trained separately to predict the clinical outcomes. Note that these baselines incorporate multimodal and dynamic information, but do not directly operate on the network structure of the connectomes. Our second baseline class omits the two step approach in lieu of an end-to-end convolutional neural network based on the work of [Kawahara et al. (2017)]. We train this model on the static rs-fMRI and DTI connectomes in tandem to predict the clinical scores. This baseline operates directly on the correlation and connectivity matrices, but ignores the dynamic evolution of functional connectivity. Next, we present the comparison of our deep sr-DDL by omitting the structural regularization. This helps us evaluate the benefit provided by the multimodal integration of DTI and rs-fMRI data.

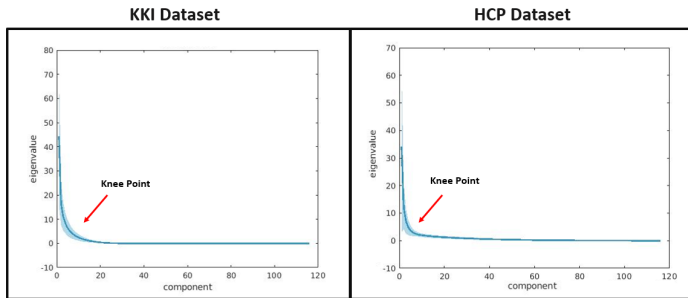


Figure 5: Scree Plot of the correlation matrices to corroborate the selected values for K . (L) KKI Dataset (R) HCP Dataset. The thick line denotes the mean eigenvalue, while the shaded area indicates the standard deviation across subjects and time points.

¹<https://github.com/Niharika-SD/Deep-sr-DDL>

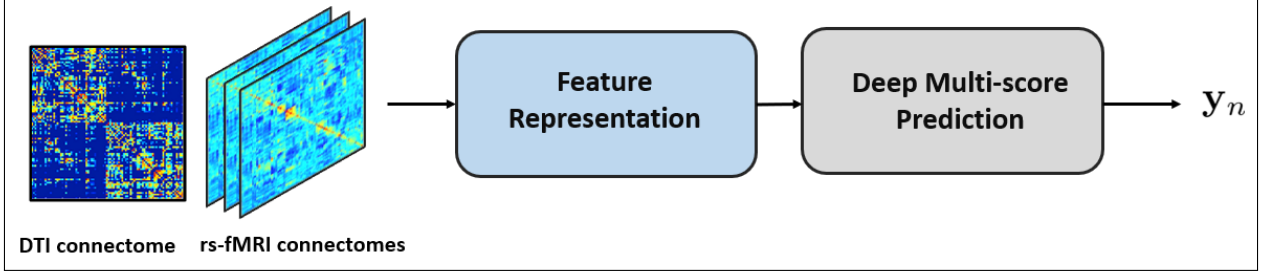


Figure 6: A typical two stage baseline. We input the dynamic correlation matrices and DTI connectomes to Stage 1, which performs Feature Extraction. This step could be a technique from machine learning, graph theory or a statistical measure. Stage 2 is a deep network that predicts the clinical scores

Our final baseline highlights the benefit of our joint optimization procedure. In this experiment, we decouple the optimization of the dynamic matrix factorization and deep network in Fig. 3 similar to the two stage pipelines.

2.3.1. Graph Theoretic Feature Selection:

Notice that the subject-specific correlation rs-fMRI matrices $\{\Gamma_n^t\}$ and the corresponding binary DTI adjacency matrices \mathbf{A}_n indicate time-varying functional and anatomical connectivity between the ROIs respectively. Therefore, we multiply the two to generate the time-varying multimodal graphs whose nodes are the brain ROIs and edges are defined by the temporal connectivity between these ROIs. We denote the corresponding adjacency matrices for these graphs by $\{\Psi_n^t = \mathbf{A}_n \circ \Gamma_n^t \in \mathcal{R}^{P \times P}\}$, where we threshold each Ψ_n^t to remove negative values. Each element $[\Psi_n^t]_{ij}$ gives the strength of association between two communicating sub-regions i and j in individual n at time t . We summarize the topology of these graphs via **Betweenness Centrality** (C_B) to obtain a time-varying estimate of brain connectivity for each ROI [Bassett and Bullmore (2006); Sporns et al. (2004)]. $C_B(v)$ for region v is calculated as:

$$C_B^t(v) = \sum_{s \neq v \neq u \in V} \frac{\sigma_{su}^t(v)}{\sigma_{su}^t} \quad (16)$$

σ_{su}^t is the total number of shortest paths from node s to node u at time t , and $\sigma_{su}^t(v)$ is the number of those paths that pass through v . This measure quantifies the number of times a node acts as a bridge along the shortest path between two other nodes and has found wide usage in characterizing small-worlded networks in brain connectivity [Sporns et al. (2004)]. We effectively reduce the dimensionality of the connectivity features. Again, the collection of features $\{C_B^t\}$ are used to train an LSTM-ANN predictor from Fig. 3 with two hidden layers having width 200 due to the higher input feature dimensionality.

2.3.2. ICA Feature Selection

This baseline employs **Independent Component Analysis (ICA)** combined an the LSTM-ANN predictor. ICA is a statistical technique that extracts representative spatial patterns from the rs-fMRI time series. It has

now become ubiquitous in fMRI analysis for its ability to identify group level differences as well as model individual-specific connectivity signatures. Essentially, ICA decomposes multivariate signals into ‘independent’ non-Gaussian components based on the data statistics.

This algorithm can be extended to the multi-subject analysis setting via Group ICA (G-ICA). Specifically, we extract independent spatial patterns common across patients, by combining the contribution of the individual time courses. For this baseline, we first perform G-ICA using the GIFT toolbox [Calhoun, Liu and Adalı (2009)], and derive independent spatial maps for each subject from their raw rs-fMRI scans. We then compute the average time courses for each spatial map considering the constituent voxels. This provides us with a feature representation of reduced dimension equal to the number of specified maps ($d \ll L$) for each individual. For our experiments, we extract 15 ICA components. These time courses are input into the LSTM-ANN network in Fig. 3 with two hidden layers of width 40 to predict the clinical outcomes.

2.3.3. BrainNet Convolutional Neural Network

The BrainNet CNN [Kawahara et al. (2017)] relies on specialized fully convolutional layers for feature extraction, and was originally used to predict cognitive and motor outcomes from DTI connectomes. Fig. 7 provides a pictorial overview of the original architecture adapted for clinical outcome prediction from multimodal data. Each branch of the network accepts as input a $P \times P$ connectome, to which it applies a cascade of two edge-edge (E-E) convolutional operations. This E-E operation combines individual convolutions acting on the row and column to which the input element belongs. It is followed by a series of edge-node (E-N) blocks that reduce the dimensionality of the intermediate outputs, followed by a node-graph (N-G) operation for pooling. Finally, the output clinical scores are predicted via a fully connected artificial neural network for regression.

We feed the rs-fMRI static connectomes ($\hat{\Gamma}_n$) and DTI Laplacians \mathbf{L}_n into two disjoint fully convolutional branches with the architecture described above. We integrate the learned features via concatenation and input them into the fully connected layers described in Fig. 7,

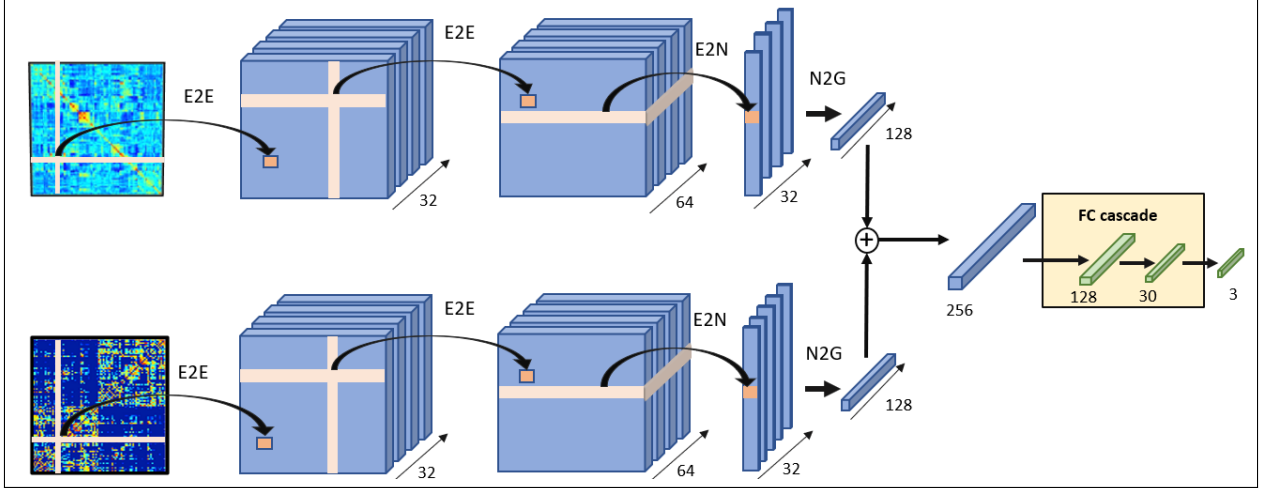


Figure 7: The BrainNet CNN baseline [Kawahara et al. (2017)] for severity prediction from multimodal data

but with the number of outputs equal to the dimensionality of the clinical severity vector \mathbf{y}_n . We set the learning rate, momentum and weight decay parameters according to the guidelines in [Kawahara et al. (2017)].

2.3.4. Deep sr-DDL without DTI regularization

In this baseline, we examine the effect of excluding the structural regularization provided by the DTI data from the joint objective in Eq. (7). The resulting objective function takes the following form:

$$\begin{aligned} \mathcal{J}_w(\mathbf{B}, \{\mathbf{c}_n^t\}, \Theta; \{\mathbf{\Gamma}_n^t\}, \{\mathbf{y}_n\}) \\ = \sum_n \sum_t \frac{1}{T_n} \|\mathbf{\Gamma}_n^t - \mathbf{B} \text{diag}(\mathbf{c}_n^t) \mathbf{B}^T\|_F^2 \\ + \lambda \sum_n \mathcal{L}(\Theta, \{\mathbf{c}_n^t\}; \mathbf{y}_n) \quad \text{s.t.} \quad \mathbf{c}_{nk}^t \geq 0, \quad \mathbf{B}^T \mathbf{B} = \mathcal{I}_K. \end{aligned} \quad (17)$$

Notice that amounts to replacing the Weighted Frobenius Norm formulation by a regular ℓ_2 penalty. This allows us to adopt the alternating minimization procedure in Section 2.2 to optimize Eq. (17) with a few minor modifications. Specifically, instead of T_n constraints per subject, we use a single constraint of the form $\mathbf{D} = \mathbf{B}$, enforced via a single Augmented Lagrangian $\mathbf{\Lambda}$. This effectively ensures that the new objective has a quadratic form in \mathbf{B} , along with a closed form update for \mathbf{D} . As before, we cycle through four individual steps, namely:

- Closed form Procrustes solution for the basis \mathbf{B}
- Updating the temporal loadings $\{\mathbf{c}_n^t\}$ (ADAM)
- Updating the Neural Network Parameters Θ (ADAM)
- Augmented Lagrangian updates for the constraint variables $\{\mathbf{D}, \mathbf{\Lambda}\}$

Similar to the Deep sr-DDL, we use $K = 15$ networks as inputs to the LSTM-ANN network with two hidden layers of width 40 to predict the clinical outcomes.

2.3.5. Decoupled Deep sr-DDL

Our final baseline examines the efficacy of our coupled optimization procedure in Section 2.2 with regards to generalization onto unseen subjects. Here, we first run the feature extraction using the sr-DDL optimization to extract the basis \mathbf{B} and temporal loadings $\{\mathbf{c}_n^t\}$. We then use the $\{\mathbf{c}_n^t\}$ as inputs to train the LSTM-ANN network in Fig. 3 to predict the scores \mathbf{y}_n . This is akin to the two-stage baselines delineated in Fig. 6.

Again, we use $K = 15$ networks with an a two layered LSTM-ANN having hidden layer width 40

3. Experimental Results:

3.1. Validation on Synthetic Data

As a sanity check, we first validate our optimization in Section 2.2 on synthetic data generated from the equivalent generative process, as captured by the graphical model in Fig. 8. This experiment allows us to assess the behavior of our algorithm under various noise scenarios. As described in Section 2.2, the observed variables are the temporal correlation matrices $\{\mathbf{\Gamma}_n^t\}$, the DTI Laplacians \mathbf{L}_n , and the clinical scores $\{\mathbf{y}_n\}$, while the latent variables are the basis \mathbf{B} , the coefficients $\{\mathbf{c}_n^t\}$, and the neural network weights Θ . Note that the dynamic correlation matrices $\{\mathbf{\Gamma}_n^t\}$ are completely described by the basis \mathbf{B} , the coefficients $\{\mathbf{c}_n^t\}$ and the Laplacian weighting \mathbf{L}_n . We further observe that the rs-fMRI data decompositions for each subject couple only through the shared basis and the clinical predictions through the shared network weights Θ . Conditioned on these variables, $\{\{\mathbf{\Gamma}_n^t\}, \mathbf{L}_n, \{\mathbf{c}_n^t\}, \Theta, \mathbf{y}_n\}$ are independent across subjects. Fig. 8 captures these conditional relationships.

We start by generating a basis matrix $\hat{\mathbf{B}} \in \mathcal{R}^{P \times K}$ by drawing its entries independently from a zero mean Gaussian with variance one. We then use the Gram-Schmidt procedure to compute an orthogonal basis $\mathbf{B}_o = \text{orth}(\hat{\mathbf{B}})$. Finally, we simulate corruptions to this basis via additive

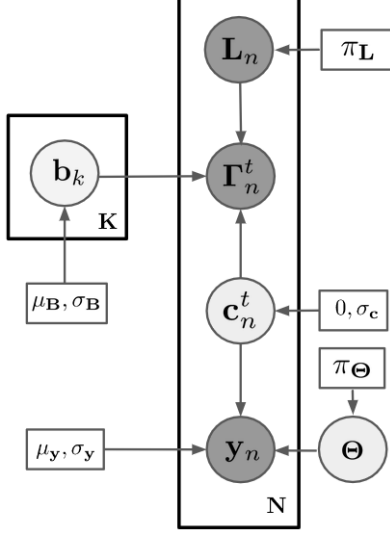


Figure 8: The graphical model for generating synthetic data. We fix the model parameters $\sigma_c = 4$, number of subjects N at 60, and number networks K at 4. The dimensionality of \mathbf{y}_n is $M = 3$ and the length of the scan $T_n = 30$ for each subject. The shaded circles denote observed variables, while the clear circles indicate latent variables.

Gaussian noise $\mathbf{B} = \mathbf{B}_o + \mathcal{N}(0, \sigma_B)$. Effectively, the value of σ_B quantifies the deviations of \mathbf{B} from orthogonality, which is an assumption of our model. Note that the coefficient values in \mathbf{c}_n are independent across networks and subjects, but not across time. Thus, for each subject, we generate the temporal coefficients using a isotropic Gaussian process with zero mean, and variance σ_c . These values are clipped at 0 to reflect the non-negativity in the coefficients. The variance parameter σ_c defines the scale of the coefficients. Next, we simulate the Graph Laplacians \mathbf{L}_n for each subject based on structural connectivity priors computed using real-world data. Specifically, for each region pair, we first create a histogram of connectivity using binary adjacency matrices from the HCP database. With π_L denoting the probability of a connection between ROI pairs, we sample a symmetric graph adjacency matrix \mathbf{A}_n per subject via a Bernoulli distribution with parameter π_L . We then compute the corresponding Laplacians \mathbf{L}_n from \mathbf{A}_n . This choice of prior helps us generate realistic structural connectivity profiles.

Now, recall that our model seeks to approximate the rs-fMRI dynamic correlation matrices by $\mathbf{\Gamma}_n^t \approx \mathbf{B} \text{diag}(\mathbf{c}_n^t) \mathbf{B}^T$. Additionally, this decomposition is regularized by the individual Laplacians \mathbf{L}_n . Since we wish to evaluate the quality of this approximation, our generative model simulates $\mathbf{\Gamma}_n^t$ by adding structured noise (parametrized by \mathbf{L}_n) to $\mathbf{B} \text{diag}(\mathbf{c}_n^t) \mathbf{B}^T$. Specifically, we use the eigenbasis \mathbf{X} of \mathbf{L}_n to generate additive noise $\mathbf{N} = \sigma_{\Gamma} \mathbf{X} \mathbf{X}^T$. We then compute the correlation matrices as $\mathbf{\Gamma}_n^t = \mathbf{B} \text{diag}(\mathbf{c}_n^t) \mathbf{B}^T + \mathbf{N}$. Note that this procedure preserves the positive semi-definiteness of the decomposition. Effectively, the parameter σ_{Γ} controls the level of

corruption in the observed dynamic correlation matrices. Finally, the observed variable $\{\mathbf{y}_n\}$, translates to a Gaussian with mean $\mu_{\mathbf{y}_n} = \mathcal{F}_{\Theta}(\{\mathbf{c}_n^t\}) \in \mathcal{R}^{M \times 1}$, and variance $\sigma_{\mathbf{y}_n} \mathbf{I}_M$. The function mapping \mathcal{F}_{Θ} refers to the LSTM-ANN network with the parameters Θ - which we randomly initialize. This is again folded to reflect positive values of \mathbf{y}_n . Here, $\sigma_{\mathbf{y}}$ controls the noise in the clinical scores.

There are two sources of noise for the observed variables. The first is error in the correlation matrices $\mathbf{\Gamma}_n^t$, controlled by changing σ_{Γ} . The second case is error in the clinical scores \mathbf{y}_n , quantified by the parameter $\sigma_{\mathbf{y}}$. Additionally, we are also interested in evaluating the performance under varying levels of deviations of the basis from orthogonality. This is controlled by the parameter σ_B .

We evaluate the efficacy of our algorithm using two separate metrics. The first is an average inner-product measure of similarity S between each recovered network, $\bar{\mathbf{b}}_k$, and its corresponding best matched ground truth network, \mathbf{b}_k , normalizing the latter to unit norm, that is:

$$S = \frac{1}{K} \sum_k \frac{|\mathbf{b}_k^T \bar{\mathbf{b}}_k|}{\|\mathbf{b}_k\|_2}. \quad (18)$$

The second metric is the Median Absolute Error (MAE) between the output of the trained LSTM-ANN $\hat{\mathbf{y}}_n$ and the true scores \mathbf{y}_n , for the score m , computed as :

$$\text{MAE} = \text{median}(|\hat{\mathbf{y}}_{:,m} - \mathbf{y}_{:,m}|), \quad (19)$$

Fig. 9 depicts the performance of the algorithm in these three cases. In the each subplots, the x -axis corresponds to increasing the levels of noise. In the first two subplots, the y -axis indicates the similarity metric S computed for the particular setting, while in the rightmost subplot, we plot the MAE for predicting the three scores. All numerical results have been aggregated over 50 independent trials.

In the leftmost plot, an x -axis value close to 0 indicates low levels of deviation of \mathbf{B} from orthogonality, while increasing values corresponds to a more severe deviation from the modeling assumptions. During this experiment, the values of the other free parameters in Fig. 8 were held constant. We observed that the MAE of the three scores remains roughly constant for all noise settings (score 1— 1.49 ± 0.09 , score 2— 1.34 ± 0.07 , score 3— 3.10 ± 0.11). The middle plot evaluates subnetwork recovery when the noise in the dynamic correlation matrices, i.e. σ_{Γ} is increased. The x -axis reports normalized values of σ_{Γ_n} while the remaining free parameters were held constant. Similar to the previous scenario, the MAE remains roughly constant for varying noise settings (score 1— 1.50 ± 0.08 , score 2— 1.50 ± 0.06 , score 3— 2.96 ± 0.50). Finally, the rightmost plot in Fig. 9 indicates performance under varying noise in the scores \mathbf{y}_n . Again, normalized $\sigma_{\mathbf{y}}$ values are reported on the x -axis. For this experiment, we observed that $S = 0.87 \pm 0.05$ for varying noise levels.

As expected, increased noise in the correlation matrices and deviations from orthogonality worsens recovery performance of the algorithm. This is reflected by the decay

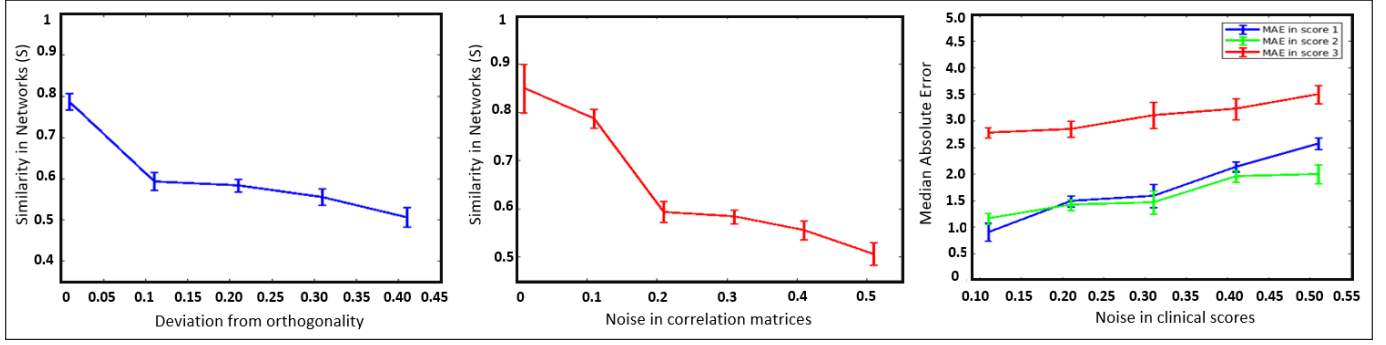


Figure 9: Performance on synthetic experiments. (L): Varying the level of deviation from orthogonality ($\sigma_{\mathbf{T}} = 0.2$, $\sigma_{\mathbf{Y}} = 0.2$), (M): Varying the level of noise in $\mathbf{\Gamma}$ ($\sigma_{\mathbf{B}} = 0.2$, $\sigma_{\mathbf{Y}} = 0.2$), (R): Varying the level of noise in \mathbf{y}_n under ($\sigma_{\mathbf{B}} = 0.2$, $\sigma_{\mathbf{T}} = 0.2$) Values on the x-axis have been normalized to reflect a $[0 - 1]$ range by dividing by the maximum value of the variable. We report deviations from the mean for recovered similarity/MAE at each parameter setting in terms of a standard error value. The reported x-axis range reflects the regimes within which the algorithm converges to a local solution

in the similarity measure along with increasing noise parameters. Since the parameter $\sigma_{\mathbf{Y}}$ is held constant, we do not observe much variation in the the MAE values upon increasing the noise. Lastly, we notice that the algorithm performs better when the level of noise in the scores is lower. This is indicated by the increasing values of MAE in the right subplot in Fig. 9. Since $\sigma_{\mathbf{B}}$ is held constant for this experiment, the metric S remains fairly constant even upon increasing the noise in the scores.

Taken together, our simulations indicate that the optimization procedure is robust in the noise regime (0.01 – 0.2) estimated from the real-world rs-fMRI data. In addition, these experiments help us identify the stable parameter settings ($\lambda = 1 - 10$) and set appropriate learning rates for the algorithm which guide our real world experiments.

3.2. Real-World Experiments: Population Studies of Connectomics and Behavior

We evaluate our deep-generative hybrid on two separate cohorts. The first dataset is a cohort of 93 healthy individuals from the Human Connectome Project (HCP) database [Van Essen, Smith, Barch, Behrens, Yacoub, Ugurbil, Consortium et al. (2013)] having both the rs-fMRI and DTI scans. We refer to this as the HCP dataset. Cognitive outcomes such as fluid intelligence are believed to be closely connected to structural (SC) and function connectivity (FC) in the human brain [Zimmermann, Griffiths and McIntosh (2018)]. Thus, jointly modeling multimodal neuroimaging and cognitive data helps exploit this fundamental interweave and uncover the neural underpinnings of cognition. Finally, we chose to focus on a small dataset ($N = 93$) to demonstrate that our framework is suitable for clinical rs-fMRI applications, many of which have limited sample sizes.

Our second dataset consists of 57 children with high functioning Autism Spectrum Disorder (ASD) acquired at the Kennedy Krieger Institute in Baltimore, USA. Henceforth, we refer to this as the KKI dataset. The age of the subjects from this cohort is 10.06 ± 1.26 with an IQ of 110 ± 14.03 . Social and communicative deficits in

ASD are believed to arise from aberrant interactions between regions of the brain that are linked by structural and functional connectivity [Rudie, Brown, Beck-Pancer, Hernandez, Dennis, Thompson, Bookheimer and Dapretto (2013)]. Thus, identifying these patterns plays a crucial role in illuminating the etiological basis of the disorder.

Neuroimaging Data. As described in [Van Essen et al. (2013)], the HCP S1200 dataset was acquired on a Siemens 3T scanner (TR/TE= 0.72ms/0.33ms, spatial resolution = $2 \times 2 \times 2$ mm). The rs-fMRI scans were processed according to the standard pre-processing pipeline described in [Smith, Beckmann, Andersson, Auerbach, Bijsterbosch, Douaud, Duff, Feinberg, Griffanti, Harms et al. (2013)], which includes additional processing to account for confounds due to motion and physiological noise. We opted to use a 15 minute interval (typical of clinical rs-fMRI studies of neurodevelopmental disorders) from the second scan of each subjects first visit for our analysis.

The DTI data from the HCP dataset was processed using the standard Neurodata MR Graphs package (ndmg) [Kiar, Roncal, Mhembe, Bridgeford, Burns and Vogelstein (2016)]. This consists of co-registration to anatomical space via FSL [Jenkinson, Beckmann, Behrens, Woolrich and Smith (2012)], followed by tensor estimation in the MNI space and probabilistic tractography to compute the fibre tracking streamlines.

For the KKI dataset, rs-fMRI acquisition was performed on a Phillips 3T Achieva scanner with a single shot, partially parallel gradient-recalled EPI sequence with TR/TE = 2500/30ms, flip angle 70° , res = $3.05 \times 3.15 \times 3$ mm, having 128 or 156 time samples. The children were instructed to relax with eyes open and focus on a central cross-hair while remaining still. We used an in-house pre-processing pipeline in [Nebel, Joel, Muschelli, Barber, Caffo, Pekar and Mostofsky (2014)] and pre-validated across several studies [DSouza et al. (2020); Nebel, Eloyan, Nettles, Sweeney, Ament, Ward, Choe, Barber, Pekar and Mostofsky (2016); Venkataraman, Wymbs, Nebel and Mostofsky (2017)]. This consists of slice time correction, rigid

body realignment, and normalization to the EPI version of the MNI template using SPM [Penny, Friston, Ashburner, Kiebel and Nichols (2011)], followed by temporal detrending of the time courses to remove gradual trends in the data. A CompCorr50 [Ciric, Rosen, Erus, Cieslak, Adenbimpe, Cook, Bassett, Davatzikos, Wolf and Satterthwaite (2018); Muschelli, Nebel, Caffo, Barber, Pekar and Mostofsky (2014)] strategy was used to estimate and remove spatially coherent noise from the white matter and ventricles, along with the linearly detrended versions of the six rigid body realignment parameters and their first derivatives, followed by spatial smoothing using a 6mm FWHM Gaussian kernel and temporal smoothing via a band pass filter (0.01 – 0.1Hz). Lastly, the data was despiked using the AFNI package [Cox (1996)].

The DTI acquisition for the KKI dataset was collected on a 3T Philips scanner (EPI, SENSE factor= 2.5, TR= 6.356s, TE= 75ms, res = $0.8 \times 0.8 \times 2.2$ mm, and FOV= 212). We collected two identical runs, each with a single b0 and 32 non-collinear gradient directions at $b = 700\text{s/mm}^2$. The data was pre-processed using the standard FDT [Jenkinson et al. (2012)] pipeline in FSL consisting of susceptibility distortion correction, followed by corrections for eddy currents, motion and outliers. From here, tensor model fitting was performed to generate the transformation matrices and extract atlas based metrics. We used the BEDPOSTx tool in FSL [Behrens, Berg, Jbabdi, Rushworth and Woolrich (2007)] to perform a bayesian estimation of the diffusion parameters at each voxel, followed by tractography using PROBTRACKx [Behrens et al. (2007)].

Our experiments rely on the Automatic Anatomical Labelling (AAL) atlas [Tzourio-Mazoyer, Landeau, Papathanassiou, Crivello, Etard, Delcroix, Mazoyer and Joliot (2002)] parcellation for the rs-fMRI and DTI data. AAL consists of 116 cortical, subcortical and cerebellar regions. We employ a sliding window protocol as shown in Fig. 2. Due to the different TR, we set the sliding window parameters to window length = 156 and stride = 17 for the HCP dataset, and window length = 45 and stride = 5 for the KKI dataset to extract dynamic correlation matrices from the 116 average time courses. We discuss the sensitivity to this choice in Section 4.1. Thus, for each individual, we have correlation matrices of size 116×116 based on the Pearson’s Correlation Coefficient between the average regional time-series. Empirically, we observed a consistent noise component with nearly unchanging contribution from all brain regions and low predictive power for both datasets. Therefore, we subtracted out the first eigenvector contribution from each of the correlation matrices and used the residuals as the inputs $\{\mathbf{T}_n\}$ to the algorithm and the baselines.

Each DTI connectivity matrix \mathbf{A}_n is binary, where $[\mathbf{A}_n]_{ij} = 1$ corresponds to the presence of at least one tract between the regions i and j , 116 in total for AAL. For the KKI dataset, we impute the DTI connectivity for the 11 individual, who do not have DTI based on the training

data in each cross validation fold.

Behavioral Data. For the HCP database, we examine the Cognitive Fluid Intelligence Score (CFIS) described in [Bilker, Hansen, Brensinger, Richard, Gur and Gur (2012); Duncan (2005)], adjusted for age. This is scored based on a battery of tests measuring cognitive reasoning, considered a nonverbal estimate of fluid intelligence in subjects. The dynamic range for the score is 70 – 150, with higher scores indicating better cognitive abilities.

We analyzed three independent measures of clinical severity for the KKI dataset. These include:

- 1 Autism Diagnostic Observation Schedule, Version 2 (ADOS-2) total raw score
- 2 Social Responsiveness Scale (SRS) total raw score
- 3 Praxis total percent correct score

The ADOS consists of several sub-scores which quantify the social-communicative deficits in individuals along with the restrictive/repetitive behaviors [Lord, Risi, Lambrecht, Cook, Leventhal, DiLavore, Pickles and Rutter (2000)]. The test evaluates the child against a set of guidelines and is administered by a trained clinician. We compute the total score by adding the individual sub-scores. The dynamic range for ADOS is between 0 – 30, with higher score indicating greater impairment.

The SRS scale quantifies the level of social responsiveness of a subject [Bölte, Poustka and Constantino (2008)]. Typically, these attributes are scored by parent/care-giver or teacher who completes a standardized questionnaire that assess various aspects of the child’s behavior. Consequently, SRS reporting tends to be more variable across subjects, as compared to ADOS, since the responses are heavily biased by the parent/teacher attitudes. The SRS dynamic range is between 70 – 200 for ASD subjects, with higher values corresponding to higher severity in terms of social responsiveness.

Finally, Praxis is assessed using the Florida Apraxia Battery (modified for children) [Mostofsky, Dubey, Jerath, Jansiewicz, Goldberg and Denckla (2006)]. It assesses the ability to perform skilled motor gestures on command, by imitation, and with actual tool use. Several studies [Mostofsky et al. (2006), Dziuk, Larson, Apostu, Mahone, Denckla and Mostofsky (2007), Dowell, Mahone and Mostofsky (2009), Nebel et al. (2016)] reveal that children with ASD show marked impairments in Praxis a.k.a., developmental dyspraxia, and that impaired Praxis correlates with impairments in core autism social-communicative and behavioral features. Performance is videotaped and later scored by two trained research-reliable raters, with total percent correctly performed gestures as the dependent variable of interest. Scores therefore range from 0–100, with higher scores indicating better Praxis performance. This measure was available for only 48 of the 57 subjects in the KKI dataset.

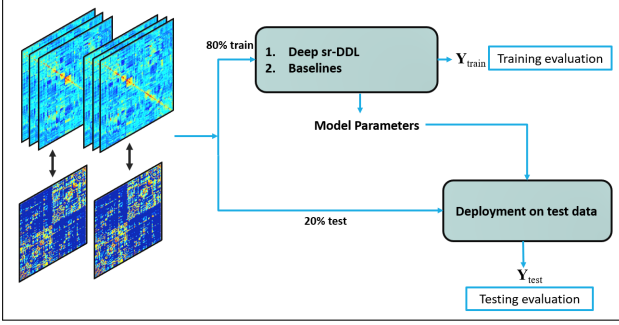


Figure 10: A five-fold cross validation for evaluating performance

3.3. Evaluating Predictive Performance

We characterize the performance of each method using a five-fold cross validation strategy, as illustrated in Fig. 10. We first randomly split the data set into five training and test folds. For each fold, we train our framework and the baselines on an 80 percent training set split of the data. Then, we use the trained models to predict the clinical scores on the held out 20 percent, which constitutes the testing set for that fold. Each example is a part of the test set in exactly one of the 5 folds.

We report two quantitative measures of performance. The first is the Median Absolute Error (MAE), defined in Eq. (19), which quantifies the absolute distance between the measured and predicted scores across individuals. Lower MAE indicates better testing performance.

The second metric is the Normalized Mutual Information (NMI), which assesses the similarity in the distribution of the predicted and observed score distributions across subjects. NMI for the score m is computed as:

$$\text{NMI}(\mathbf{y}_{:,m}, \hat{\mathbf{y}}_{:,m}) = \frac{H(\mathbf{y}_{:,m}) + H(\hat{\mathbf{y}}_{:,m}) - H(\mathbf{y}_{:,m}, \hat{\mathbf{y}}_{:,m})}{\min\{H(\mathbf{y}_{:,m}), H(\hat{\mathbf{y}}_{:,m})\}}$$

Here, $H(\mathbf{y}_{:,m})$ is the entropy of $\mathbf{y}_{:,m}$ and $H(\mathbf{y}_{:,m}, \hat{\mathbf{y}}_{:,m})$ is the joint entropy between $\mathbf{y}_{:,m}$ and $\hat{\mathbf{y}}_{:,m}$. NMI ranges between 0–1 with a higher value indicating better agreement between predicted and measured score distributions, and thus characterizing improved performance.

3.4. Multi-Score Prediction on Real World Data

Similarly, Fig. 11 illustrates the performance comparison of our deep sr-DDL framework against the baselines in Section 2.3 on the HCP dataset for predicting the CFIS. Fig. 12 presents the same comparison on the KKI dataset for multi-score prediction. In each figure, the scores predicted by the algorithm are plotted on the \mathbf{y} -axis against the measured ground truth score on the \mathbf{x} -axis. The bold $\mathbf{x} = \mathbf{y}$ line represents ideal performance. The red points represent the training data, while the blue points indicate the held out testing data for all the cross validation folds.

We observe that the training performance of the baselines is good (i.e. the red points follow the $\mathbf{x} = \mathbf{y}$ line) in all cases for both datasets. However, in case of testing performance, our method outperforms the baselines in all

cases. This performance gain is particularly pronounced in the case of multiscore prediction (KKI dataset). Empirically, we are able to tune the baseline hyperparameters to obtain good testing performance on the KKI dataset for a single score (ADOS), but the prediction of the remaining scores (SRS and Praxis for the KKI dataset) suffers. Notice that the prediction on SRS, Praxis (KKI dataset) and CFIS (HCP dataset) hovers around the population mean of the score in almost all cases. Finally, we notice that omitting the structural regularization from the deep sr-DDL performs worse than our method.

In contrast to the baselines, the testing predictions of our framework follow the $\mathbf{x} = \mathbf{y}$ more closely. The machine learning, statistical and graph theoretic techniques we selected for a comparison are well known in literature for being able to robustly provide compact characterizations for high dimensional datasets. However, we see that ICA is unable to estimate a reliable projection of the data that is particularly useful for behavioral prediction. Similarly, the betweenness centrality measure is unable to extract informative topologies for brain-behavior integration. We conjecture that the aggregate nature of this measure is useful for capturing group-level commonalities, but falls short of modeling subject-specific differences. Furthermore, even the BrainNet CNN, which directly exploits the graph structure of the connectomes falls short of generalizing to multi-score prediction. Additionally, it ignores the dynamic information in the rs-fMRI data. In case of the baseline where we omit the structural regularization, i.e. deep sr-DDL without DTI, we notice that the method learns a representation of the rs-fMRI data that generalizes beyond the training set, but still falls short of the performance when anatomical information is included. This clearly demonstrates the benefit of supplementing the functional data with structural priors. Finally, the failure of the decoupled dynamic matrix factorization and deep-network makes a strong case for jointly optimizing the neuroimaging and behavioral representations. The basis estimated independently of behavior are not indicative of clinical outcomes, due to which the regression performance suffers. We also quantify the performance indicated in these figures in Table 1 (HCP dataset) and Table 2 (KKI dataset) based on the MAE and NMI.

Our deep sr-DDL framework explicitly optimizes for a viable tradeoff between multimodal and dynamic connectivity structures and behavioral data representations jointly. The dynamic matrix decomposition simultaneously models the group information through the basis, and the subject-specific differences through the time-varying coefficients. The DTI Laplacians streamline this decomposition to focus on anatomically informed functional pathways. The LSTM-ANN directly models the temporal variation in the coefficients, with its weights encoding representations closely interlinked with behavior. The limited number of basis elements help provide compact representations explaining the connectivity information well. The regularization and constraints ensure that the problem is

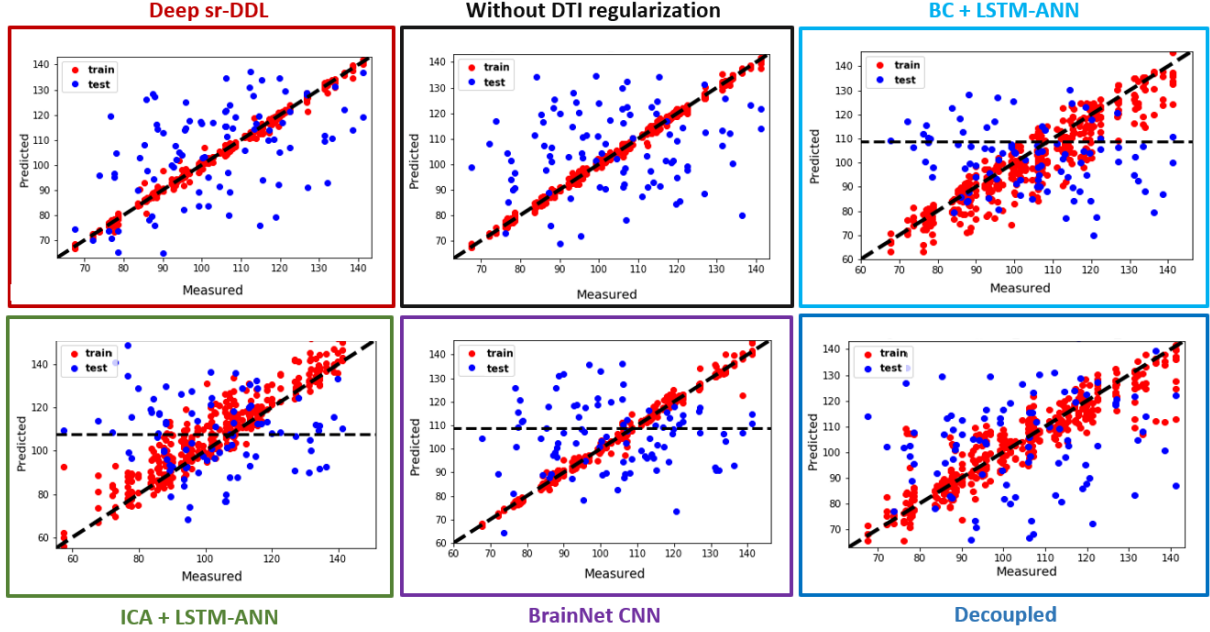


Figure 11: **HCP dataset:** Prediction performance for the Cognitive Fluid Intelligence Score by the **Red Box:** Deep sr-DDL. **Black Box:** Deep sr-DDL model without DTI regularization **Light Blue Box:** Betweenness Centrality on DTI + dynamic rs-fMRI multimodal graphs followed by LSTM-ANN predictor **Green Box:** ICA timeseries followed by LSTM-ANN predictor **Purple Box:** Branched BrainNet CNN [Kawahara et al. (2017)] on DTI and rs-fMRI static graphs **Blue Box:** Decoupled DDL factorization followed by LSTM-ANN predictor

Score	Method	MAE Train	MAE Test	NMI Train	NMI Test
CFIS	BC & LSTM-ANN	4.12	16.89	0.80	0.57
	ICA & LSTM-ANN	4.54	20.02	0.82	0.70
	BrainNet CNN	0.54	16.36	0.99	0.54
	Decoupled	3.31	17.21	0.80	0.71
	Without DTI regularization	0.72	16.41	0.98	0.79
	Deep sr-DDL	0.39	14.57	0.99	0.79

Table 1: **HCP Dataset:** Performance evaluation using **Median Absolute Error (MAE)** and **Normalized Mutual Information (NMI)** fit, both for testing and training. Lower MAE and higher NMI score indicate better performance. We have highlighted the best performance in bold.

well posed, yet extracts clinically meaningful representations.

3.5. Clinical Interpretation

Subnetwork Identification. Fig. 13 and Fig. 14 illustrate the 15 subnetworks in **B** trained on the HCP and the KKI dataset respectively. Each column of the basis consists of a set of co-activated subregions. We plot the values stored in these columns onto the corresponding ROIs in the AAL atlas. The colorbar in the figure indicates subnetwork contribution to the AAL regions. Regions storing negative values (cold colors) are anticorrelated with regions storing positive ones (hot colors).

Examining the subnetworks in Fig. 13, we notice that Subnetworks 9 and 3 exhibit positive and competing contributions from regions of the Default Mode Network (DMN), which has been widely inferred in the resting state literature [Raichle (2015)] and is believed to play a critical

role in consolidating memory [Sestieri, Corbetta, Romani and Shulman (2011)], as also in self-referencing and in the theory of mind [Andrews-Hanna (2012)]. At the same time, Subnetworks 3 and 4 have contributions from regions in the Frontoparietal Network (FPN). The FPN is known to be involved in executive function and goal-oriented, cognitively demanding tasks [Uddin, Yeo and Spreng (2019)]. Subnetworks 1, 10, and 15 are comprised of regions from the Medial Frontal Network (MFN), while Subnetworks 12 and 6 exhibit competing contributions from these regions. The MFN and FPN are known to play a key role in decision making, attention and working memory [Euston, Gruber and McNaughton (2012); Menon (2011)], which are directly associated with cognitive intelligence. Subnetworks 2, 8, 12, 6 and 3 include subcortical and cerebellar regions, while subnetworks 3 and 4 include contributions from the Somatomotor Network (SMN). Taken together, these networks are believed to be important functional

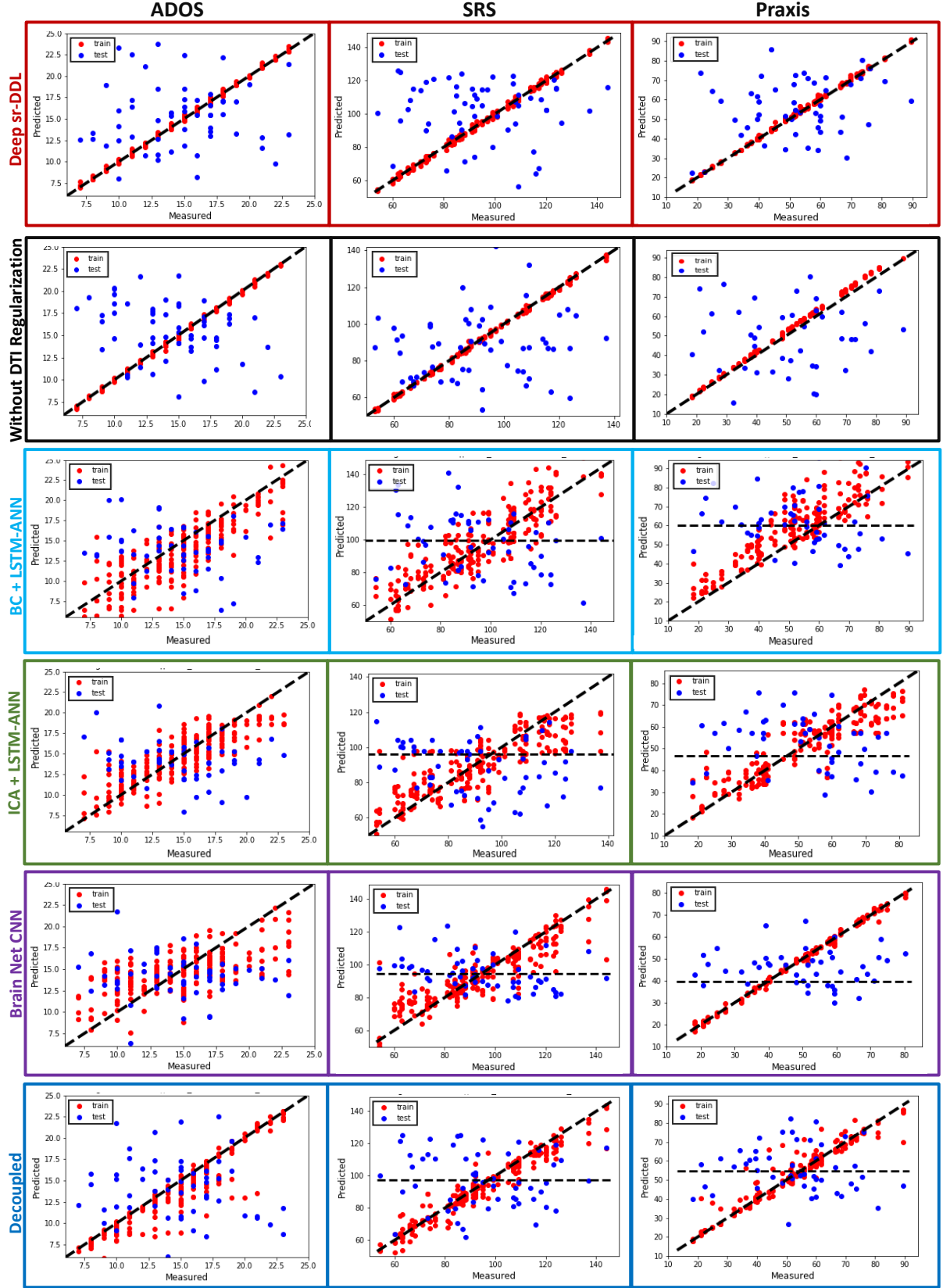


Figure 12: **KKI dataset**: Multiscore prediction performance for the (L) ADOS, (M) SRS, and (R) Praxis by the **Red Box**: Deep sr-DDL **Black Box**: Model without DTI regularization **Light Blue Box**: Betweenness Centrality on DTI + dynamic rs-fMRI multimodal graphs followed by LSTM-ANN predictor **Green Box**: ICA timeseries followed by the LSTM-ANN predictor **Purple Box**: Branched BrainNet CNN [Kawahara et al. (2017)] on DTI Laplacian and rs-fMRI static graphs **Blue Box**: Decoupled DDL factorization followed by LSTM-ANN predictor

Score	Method	MAE Train	MAE Test	NMI Train	NMI Test
ADOS	BC & LSTM-ANN	1.53	3.24	0.36	0.20
	ICA & LSTM-ANN	1.21	3.30	0.42	0.32
	BrainNet CNN	1.90	3.50	0.96	0.25
	Decoupled	1.34	3.93	0.68	0.29
	Without DTI regularization	0.13	3.27	0.99	0.26
	Deep sr-DDL	0.08	2.84	0.99	<u>0.34</u>
SRS	BC & LSTM-ANN	6.3	22.70	0.80	0.61
	ICA & LSTM-ANN	6.7	25.40	0.80	0.58
	BrainNet CNN	5.25	18.96	0.83	0.75
	Decoupled	2.10	21.45	0.76	0.78
	Without DTI regularization	0.49	18.70	0.97	0.55
	Deep sr-DDL	<u>0.51</u>	17.81	0.98	0.88
Praxis	BC & LSTM-ANN	8.10	21.10	0.53	0.79
	ICA & LSTM-ANN	5.20	22.02	0.76	0.49
	BrainNet CNN	3.78	15.15	0.95	0.19
	Decoupled	1.57	21.67	0.75	0.25
	Without DTI regularization	1.09	17.34	0.99	0.49
	Deep sr-DDL	0.13	13.50	0.99	0.85

Table 2: **KKI Dataset:** Performance evaluation using **Median Absolute Error (MAE)** and **Normalized Mutual Information (NMI)** fit, both for testing and training. Lower MAE and higher NMI score indicate better performance. We have highlighted the best performance in bold. Near misses have been underlined.

connectivity biomarkers of cognitive intelligence and consistently appear in previous literature on the HCP dataset

[Chén, Cao, Reinen, Qian, Gou, Phan, De Vos and Cannon (2019); Hearne, Mattingley and Cocchi (2016)].

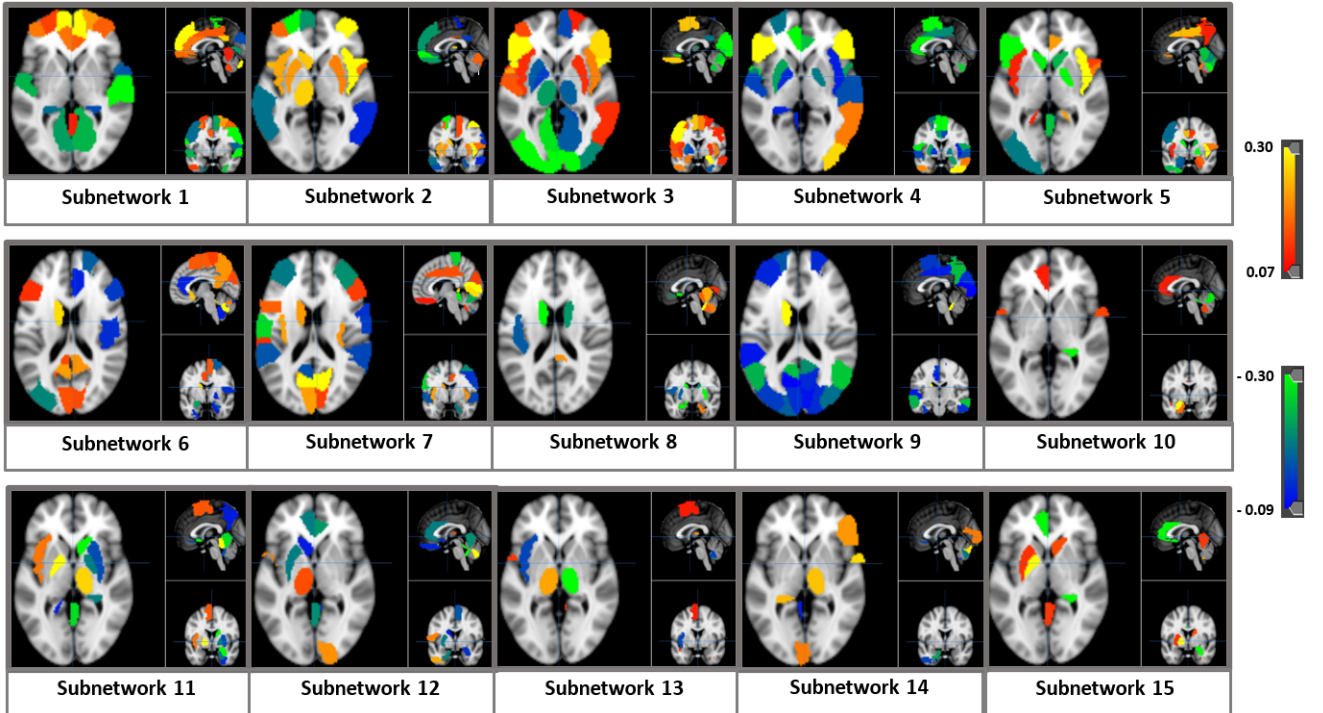


Figure 13: Complete set of subnetworks identified by the deep sr-DDL model for the HCP database. The red and orange regions are anti-correlated with the blue and green regions.

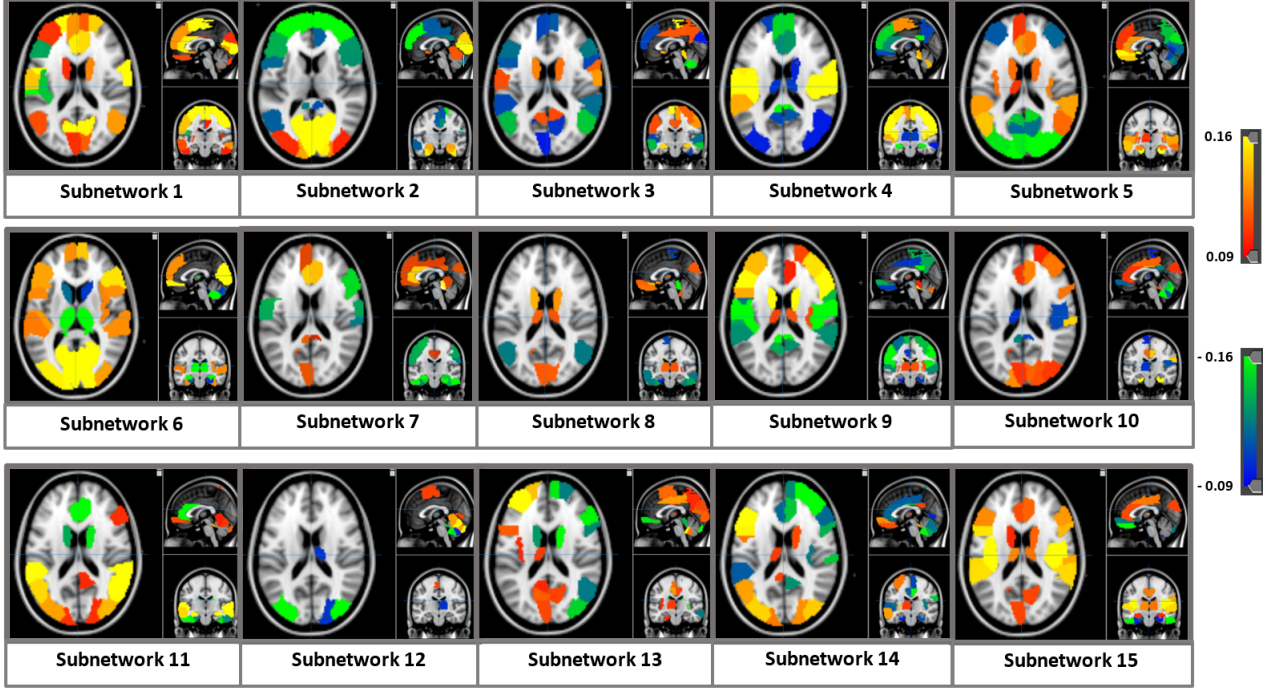


Figure 14: Complete set of subnetworks identified by the deep sr-DDL model for the KKI database. The red and orange regions are anti-correlated with the blue and green regions.

For the KKI dataset, in Fig. 14, Subnetwork 1 includes regions from the DMN, and the SMN. Similarly, Subnetwork 4 includes competing contributions from the SMN and DMN regions. Aberrant connectivity within the DMN and SMN regions have previously been reported in ASD [Lynch, Uddin, Supekar, Khouzam, Phillips and Menon (2013); Nebel et al. (2016)]. Subnetworks 2 and 12 exhibit contributions from higher order visual processing areas in the occipital and temporal lobes along with and sensorimotor regions. At the same time, Subnetworks 7 and 14 exhibits competing contributions from these areas. These findings concur with behavioral reports of reduced visual-motor integration in autism [Nebel et al. (2016)]. Subnetworks 3 and 4 exhibit anticorrelated contributions from the central executive control network (CEN) and insula. Subnetwork 6 also exhibits CEN contributions. These regions are believed to be essential for switching between goal-directed and self-referential behavior [Sridharan, Levitin and Menon (2008)]. Subnetwork 4 and Subnetwork 7 includes prefrontal and DMN regions, along with subcortical areas such as the thalamus, amygdala and hippocampus. The hippocampus is known to play a crucial role in the consolidation of long and short term memory, along with spatial memory to aid navigation. Altered memory functioning has been shown to manifest in children diagnosed with ASD [Williams, Goldstein and Minshew (2006)]. The thalamus is responsible for relaying sensory and motor signals to the cerebral cortex in the brain and has been implicated in autism-associated sensory dysfunction, a core feature of ASD [Cascio, McGlone, Folger, Tannan, Baranek,

Pelphrey and Essick (2008)]. Along with the amygdala, which is known to be associated with emotional responses, these areas may be crucial for social-emotional regulation in ASD. [Pouw, Rieffe, Stockmann and Gadow (2013)].

Finally, we observed an average similarity of 0.85 ± 0.05 and 0.81 ± 0.06 for these subnetworks across their cross validation runs on the HCP and KKI datasets respectively. This suggests that our deep-generative framework is able to capture stable underlying mechanisms which robustly explain the different sets of deficits in ASD as well robustly extract signatures of cognitive flexibility in neurotypical individuals.

Decoding *rs-fMRI* networks dynamics. Our deep sr-DDL allows us to map the evolution of functional networks in the brain by probing the LSTM-ANN representation. Recall that our model does not require the *rs-fMRI* scans to be of equal length. Fig. 15 (left) illustrates the learned attentions output by the A-ANN for the 93 subjects from the HCP dataset on the top and the 57 KKI subjects on the bottom during testing. For the KKI dataset, the patients with shorter scans have been grouped in the top of the figure. These time-points have been blackened at the beginning of the scan. The colorbar indicates the strength of the attention weights. Higher attention weights denote intervals of the scan considered especially relevant for prediction. Notice that the network highlights the start of the scan for several individuals, while it prefers focusing on the end of the scan for some others, especially pronounced in case of the KKI dataset. The patterns are comparatively more diffused for subjects in the HCP dataset, although

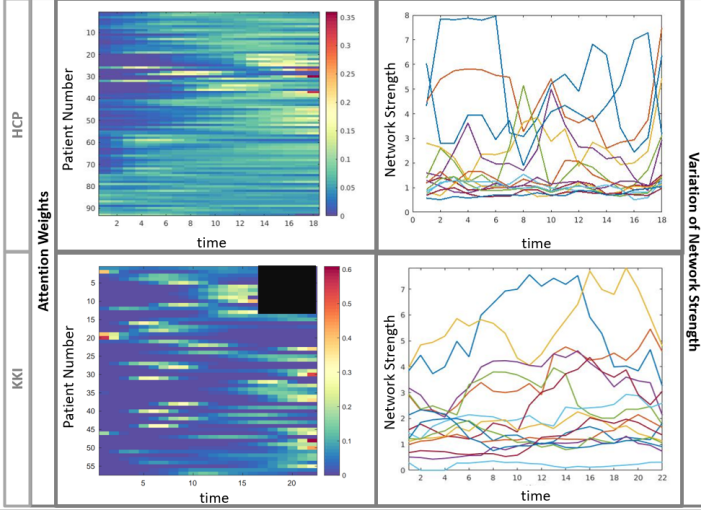


Figure 15: **(Left)** Learned attention weights **(Right)** Variation of network strength over time on the **(Top)** HCP dataset **(Bottom)** KKI dataset

several subjects manifest selectivity in terms of relevant attention weights. This is indicative of the underlying individual-level heterogeneity in both the cohorts.

Next, we illustrate the variation of the network strength for a representative Subject from the HCP dataset and KKI dataset over the scan duration in Fig. 15 (right) at the top and bottom respectively. Each solid colored line corresponds to one of the 15 sub-networks in Fig. 14. Notice that, over the scan duration, each network cycles through phases of activity and relative inactivity. Consequently, only a few networks at each time step contribute to the patient’s dynamic connectivity profile. This parallels the transient brain-states hypothesis in dynamic rs-fMRI connectivity [Allen, Damaraju, Plis, Erhardt, Eichele and Calhoun (2014)], with active states as corresponding sub-networks in the basis matrix \mathbf{B} .

4. Discussion

Our deep-generative hybrid cleverly exploits the intrinsic structure of the rs-fMRI correlation matrices through the dynamic dictionary representation to simultaneously capture group-level and subject-specific information. At the same time, the LSTM-ANN network models the temporal evolution of the rs-fMRI data to predict behavior. The compactness of our representation serves as a dimensionality reduction step that is related to the clinical score of interest, unlike the pipelined treatment commonly found in the literature. Our structural regularization helps us fold in anatomical information to guide the functional decomposition. Overall, our framework outperforms a variety of state-of-the-art graph theoretic, statistical and deep learning baselines on two separate real world datasets.

We conjecture that the baseline techniques fail to extract representative patterns from structural and functional data. These techniques are quite successful at mod-

elling group level information, but fail to generalize to the entire spectrum of cognitive, symptomatic or connectivity level differences among subjects. Consequently, they overfit the training data. Further, we demonstrate that the model is fairly robust to the choice of hyperparameters, and provide guidelines to set these for future applications of our method.

4.1. Robustness to Hyperparameter Selection

Our deep sr-DDL framework has only two free hyperparameters. The first is the number of subnetworks in \mathbf{B} . As described in Section 2.2.1, we use the eigen-spectrum of $\{\mathbf{\Gamma}_n^t\}$ to fix this at 15 for both datasets. The second is the penalty parameter λ , which controls the trade-off between representation and prediction. In addition to the model, our sliding window protocol in Fig. 2 is defined by two parameters, i.e. the sliding window length and the stride. Together, these balance the context size and information overlap within the rs-fMRI correlation matrices $\{\mathbf{\Gamma}_n^t\}$.

In this section, we evaluate the performance of our framework under three scenarios. Specifically, we sweep λ , the window length and the stride parameter independently, keeping the other two values fixed. We use five fold cross validation with the MAE metric to quantify the multi-score prediction performance, which as shown in Section 3.2, is more challenging than single score prediction. Fig. 16 plots the performance for the three scores on the KKI dataset with MAE value for each score on the y axis and the parameter value on the x axis. The operating point indicates the settings chosen in Section 3.4.

We observed that our method gives stable performance for fairly large ranges of each parameter settings. As expected, low values of λ (0.01 – 1) result in higher MAE values, likely due to underfitting. Similarly, higher values (> 6) result in overfitting to the training dataset, degrading the generalization performance. Additionally, lower values of window lengths result in higher variance among the correlation values due to noise, and hence less reliable estimates of dynamic connectivity [Lindquist (2016)]. On the other hand, very large context windows tend to miss nuances in the dynamic evolution of the scan. Empirically, we observe that a mid-range of window length 100 – 125s yields a good tradeoff between representation and prediction. The training of LSTM networks with very long sequence lengths is known to be particularly challenging owing to vanishing/exploding gradient issues during back-propagation. However, having too short a sequence confounds a reliable estimation of the LSTM weights from limited data. The stride parameter helps mitigate these issue by compactly summarizing the information in the sequence while simultaneously controlling the overlap across subsequent samples. Our experiments found a stride length between 10 – 20s to be suitable for our application.

In summary, the guidelines we identified for each of the parameters are- $\lambda \in (2 - 5)$, window length $\in (100 - 125)s$, and stride $\in (10 - 20)s$. Additionally, our experiments on the HCP dataset using the same settings indicate that

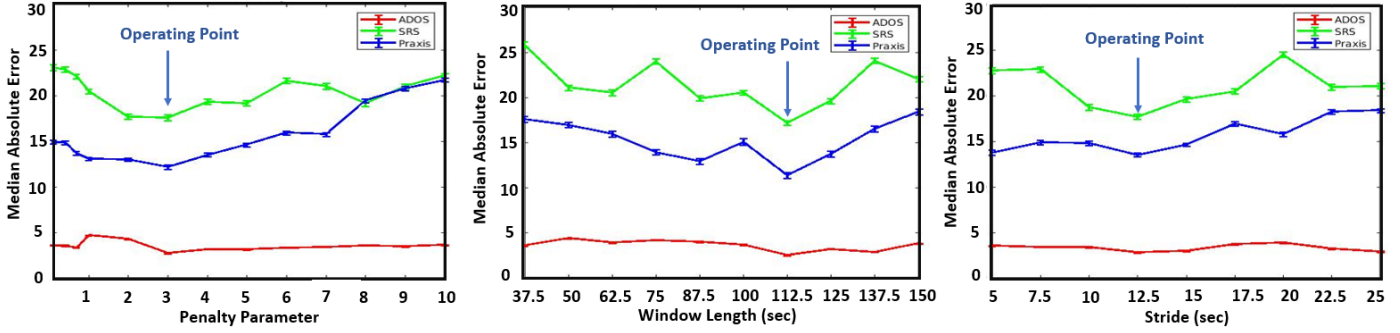


Figure 16: Performance of the Deep-Generative Hybrid upon varying (L): the penalty parameter λ (B): window length (R): stride. The highlighted yellow sections indicate a stable operating range. Our operating point is indicated by the blue arrow

the results of our method are reproducible across different populations.

4.2. Applications and Future Scope

As seen in our experiments on the in Section 3.4, our method is able to extract key predictive resting state biomarkers from healthy and autistic populations. This could potentially be useful for developing and testing the efficacy of behavioral therapies to improve treatment options for the 1 in every 68 children diagnosed with ASD. At the same time, our deep sr-DDL makes minimal assumptions. Provided we have access to a valid set of structural and functional connectivity measures and clinical scores, this analysis can be easily adapted to other neurological disorders and even predictive network models outside the medical realm. Overall, these findings greatly broaden the scope of our method for future applications.

We recognize that our model is simplistic in its assumptions, particularly in the formulation of the sr-DDL objective. More concretely, the DTI priors guide a data-driven classical rs-fMRI matrix decomposition in a regularization framework. This deliberate modelling choice conveniently preserves interpretability in the basis and simplifies the inference procedure, while making minimal assumptions about the underlying brain organization. In recent years, graph neural networks have shown great promise in brain connectivity research due to their ability to capture subtle interactions between communicating brain regions while exploiting the underlying hierarchy of brain organization. Consequently, they are emerging as important tools to probe complex pathologies in brain functioning and diagnose neurodevelopmental disorders [Anirudh and Thiagarajan (2019); Parisot, Ktena, Ferrante, Lee, Guerrero, Glocker and Rueckert (2018)]. In the future, we are exploring end-to-end graph convolutional networks that model the evolution of rs-fMRI signals on the underlying anatomical DTI graphs. In light of our current and future explorations, we hope to inch closer to a loftier goal of improving personalized healthcare.

5. Conclusion

We have introduced a novel deep-generative framework to integrate complementary information from the functional and structural neuroimaging domains, which simultaneously maps to behavior. Our unique structural regularization elegantly injects anatomical information into the rs-fMRI functional decomposition, thus providing us with an interpretable brain basis. Our deep network (LSTM-ANN) not only models the temporal variation among individuals, but also helps isolate key dynamic resting-state signatures, indicative of clinical/cognitive impairments. Our coupled optimization procedure ensures that we learn effectively from limited training data while generalizing well to unseen subjects. Finally, our framework makes very few assumptions and can potentially be applied to study other neuropsychiatric disorders (eg. ADHD, Schizophrenia) as an effective diagnostic tool.

Acknowledgements. This work has generously been supported by the National Science Foundation CRCNS award 1822575 and CAREER award 1845430, the National Institute of Mental Health (R01 MH085328-09, R01 MH078160-07, K01 MH109766 and R01 MH106564), the National Institute of Neurological Disorders and Stroke (R01NS048527-08), and the Autism Speaks foundation.

References

- Aghdam, M.A., Sharifi, A., Pedram, M.M., 2018. Combination of rs-fmri and smri data to discriminate autism spectrum disorders in young children using deep belief network. *Journal of digital imaging* 31, 895–903.
- Aielli, G.P., 2013. Dynamic conditional correlation: on properties and estimation. *Journal of Business & Economic Statistics* 31, 282–299.
- Allen, E.A., Damaraju, E., Plis, S.M., Erhardt, E.B., Eichele, T., Calhoun, V.D., 2014. Tracking whole-brain connectivity dynamics in the resting state. *Cerebral cortex* 24, 663–676.
- Andrews-Hanna, J.R., 2012. The brains default network and its adaptive role in internal mentation. *The Neuroscientist* 18, 251–270.
- Andrews-Hanna, J.R., Snyder, A.Z., Vincent, J.L., Lustig, C., Head, D., Raichle, M.E., Buckner, R.L., 2007. Disruption of large-scale brain systems in advanced aging. *Neuron* 56, 924–935.

- Anirudh, R., Thiagarajan, J.J., 2019. Bootstrapping graph convolutional neural networks for autism spectrum disorder classification, in: ICASSP 2019-2019 IEEE International Conference on Acoustics, Speech and Signal Processing (ICASSP), IEEE. pp. 3197–3201.
- Assaf, Y., Pasternak, O., 2008. Diffusion tensor imaging (dti)-based white matter mapping in brain research: a review. *Journal of molecular neuroscience* 34, 51–61.
- Atasoy, S., Donnelly, I., Pearson, J., 2016. Human brain networks function in connectome-specific harmonic waves. *Nature communications* 7, 10340.
- Banerjee, A., Jost, J., 2008. On the spectrum of the normalized graph laplacian. *Linear algebra and its applications* 428, 3015–3022.
- Bardella, G., Bifone, A., Gabrielli, A., Gozzi, A., Squartini, T., 2016. Hierarchical organization of functional connectivity in the mouse brain: a complex network approach. *Scientific reports* 6, 32060.
- Bassett, D.S., Bullmore, E., 2006. Small-world brain networks. *The neuroscientist* 12, 512–523.
- Behrens, T.E., Berg, H.J., Jbabdi, S., Rushworth, M.F., Woolrich, M.W., 2007. Probabilistic diffusion tractography with multiple fibre orientations: What can we gain? *Neuroimage* 34, 144–155.
- Bilker, W.B., Hansen, J.A., Brensinger, C.M., Richard, J., Gur, R.E., Gur, R.C., 2012. Development of abbreviated nine-item forms of the ravens standard progressive matrices test. *Assessment* 19, 354–369.
- Bölte, S., Poustka, F., Constantino, J.N., 2008. Assessing autistic traits: cross-cultural validation of the social responsiveness scale (srs). *Autism Research* 1, 354–363.
- Bowman, F.D., Zhang, L., Derado, G., Chen, S., 2012. Determining functional connectivity using fmri data with diffusion-based anatomical weighting. *NeuroImage* 62, 1769–1779.
- Bullmore, E., Sporns, O., 2009. Complex brain networks: graph theoretical analysis of structural and functional systems. *Nature Reviews Neuroscience* 10, 186.
- Cabral, J., Kringelbach, M.L., Deco, G., 2017. Functional connectivity dynamically evolves on multiple time-scales over a static structural connectome: Models and mechanisms. *NeuroImage* 160, 84–96.
- Cai, B., Zille, P., Stephen, J.M., Wilson, T.W., Calhoun, V.D., Wang, Y.P., 2017. Estimation of dynamic sparse connectivity patterns from resting state fmri. *IEEE transactions on medical imaging* 37, 1224–1234.
- Calhoun, V.D., Liu, J., Adalı, T., 2009. A review of group ica for fmri data and ica for joint inference of imaging, genetic, and erp data. *Neuroimage* 45, S163–S172.
- Caporin, M., McAleer, M., 2013. Ten things you should know about the dynamic conditional correlation representation. *Econometrics* 1, 115–126.
- Cascio, C., McGlone, F., Folger, S., Tannan, V., Baranek, G., Pelphrey, K.A., Essick, G., 2008. Tactile perception in adults with autism: a multidimensional psychophysical study. *Journal of autism and developmental disorders* 38, 127–137.
- Chén, O.Y., Cao, H., Reinen, J.M., Qian, T., Gou, J., Phan, H., De Vos, M., Cannon, T.D., 2019. Resting-state brain information flow predicts cognitive flexibility in humans. *Scientific reports* 9, 1–16.
- Ciric, R., Rosen, A.F., Erus, G., Cieslak, M., Adebimpe, A., Cook, P.A., Bassett, D.S., Davatzikos, C., Wolf, D.H., Satterthwaite, T.D., 2018. Mitigating head motion artifact in functional connectivity mri. *Nature protocols* 13, 2801–2826.
- Cox, R.W., 1996. Afni: software for analysis and visualization of functional magnetic resonance neuroimages. *Computers and Biomedical research* 29, 162–173.
- Cuingnet, R., Glaunès, J.A., Chupin, M., Benali, H., Colliot, O., 2012. Spatial and anatomical regularization of svm: a general framework for neuroimaging data. *IEEE transactions on pattern analysis and machine intelligence* 35, 682–696.
- Dowell, L.R., Mahone, E.M., Mostofsky, S.H., 2009. Associations of postural knowledge and basic motor skill with dyspraxia in autism: implication for abnormalities in distributed connectivity and motor learning. *Neuropsychology* 23, 563.
- D’Souza, N.S., Nebel, M.B., Crocetti, D., Wymbs, N., Robinson, J., Mostofsky, S., Venkataraman, A., 2020. A deep-generative hybrid model to integrate multimodal and dynamic connectivity for predicting spectrum-level deficits in autism. *arXiv preprint arXiv:2007.01931*.
- D’Souza, N.S., Nebel, M.B., Wymbs, N., Mostofsky, S., Venkataraman, A., 2018. A generative-discriminative basis learning framework to predict clinical severity from resting state functional mri data, in: *International Conference on Medical Image Computing and Computer-Assisted Intervention*, Springer. pp. 163–171.
- Duncan, J., 2005. Frontal lobe function and general intelligence: why it matters. *Cortex: A Journal Devoted to the Study of the Nervous System and Behavior*.
- Dziuk, M., Larson, J.G., Apostu, A., Mahone, E., Denckla, M., Mostofsky, S., 2007. Dyspraxia in autism: association with motor, social, and communicative deficits. *Developmental Medicine & Child Neurology* 49, 734–739.
- DSouza, N., Nebel, M., Wymbs, N., Mostofsky, S., Venkataraman, A., 2020. A joint network optimization framework to predict clinical severity from resting state functional mri data. *NeuroImage* 206, 116314.
- DSouza, N.S., Nebel, M.B., Wymbs, N., Mostofsky, S., Venkataraman, A., 2019a. A coupled manifold optimization framework to jointly model the functional connectomics and behavioral data spaces, in: *International Conference on Information Processing in Medical Imaging*, Springer. pp. 605–616.
- DSouza, N.S., Nebel, M.B., Wymbs, N., Mostofsky, S., Venkataraman, A., 2019b. Integrating neural networks and dictionary learning for multidimensional clinical characterizations from functional connectomics data, in: *International Conference on Medical Image Computing and Computer-Assisted Intervention*, Springer. pp. 709–717.
- Eavani, H., Satterthwaite, T.D., Filipovych, R., Gur, R.E., Gur, R.C., Davatzikos, C., 2015. Identifying sparse connectivity patterns in the brain using resting-state fmri. *Neuroimage* 105, 286–299.
- Engle, R., 2002. Dynamic conditional correlation: A simple class of multivariate generalized autoregressive conditional heteroskedasticity models. *Journal of Business & Economic Statistics* 20, 339–350.
- Euston, D.R., Gruber, A.J., McNaughton, B.L., 2012. The role of medial prefrontal cortex in memory and decision making. *Neuron* 76, 1057–1070.
- Everson, R., 1998. Orthogonal, but not orthonormal, procrustes problems. *Advances in computational Mathematics* 3.
- Feng, C.M., Gao, Y.L., Liu, J.X., Zheng, C.H., Yu, J., 2017. Pca based on graph laplacian regularization and p-norm for gene selection and clustering. *IEEE transactions on nanobioscience* 16, 257–265.
- Fox, M.D., Raichle, M.E., 2007. Spontaneous fluctuations in brain activity observed with functional magnetic resonance imaging. *Nature reviews neuroscience* 8, 700.
- Fukushima, M., Betzel, R.F., He, Y., van den Heuvel, M.P., Zuo, X.N., Sporns, O., 2018. Structure–function relationships during segregated and integrated network states of human brain functional connectivity. *Brain Structure and Function* 223, 1091–1106.
- Glorot, X., Bordes, A., Bengio, Y., 2011. Deep sparse rectifier neural networks, in: *Proceedings of the fourteenth international conference on artificial intelligence and statistics*, pp. 315–323.
- Goble, D.J., Coxon, J.P., Van Impe, A., Geurts, M., Van Hecke, W., Sunaert, S., Wenderoth, N., Swinnen, S.P., 2012. The neural basis of central proprioceptive processing in older versus younger adults: an important sensory role for right putamen. *Human brain mapping* 33, 895–908.
- Hahn, K., Myers, N., Prigarin, S., Rodenacker, K., Kurz, A., Förstl, H., Zimmer, C., Wohlschläger, A.M., Sorg, C., 2013. Selectively and progressively disrupted structural connectivity of functional brain networks in alzheimer’s disease revealed by a novel framework to analyze edge distributions of networks detecting disruptions with strong statistical evidence. *Neuroimage* 81, 96–109.
- Hearne, L.J., Mattingley, J.B., Cocchi, L., 2016. Functional brain

- networks related to individual differences in human intelligence at rest. *Scientific reports* 6, 32328.
- Higgins, I.A., Kundu, S., Guo, Y., 2018. Integrative bayesian analysis of brain functional networks incorporating anatomical knowledge. *Neuroimage* 181, 263–278.
- Honey, C., Sporns, O., Cammoun, L., Gigandet, X., Thiran, J.P., Meuli, R., Hagmann, P., 2009. Predicting human resting-state functional connectivity from structural connectivity. *Proceedings of the National Academy of Sciences* 106, 2035–2040.
- Jenkinson, M., Beckmann, C.F., Behrens, T.E., Woolrich, M.W., Smith, S.M., 2012. Fsl. *Neuroimage* 62, 782–790.
- Kaiser, M.D., Hudac, C.M., Shultz, S., Lee, S.M., Cheung, C., Berken, A.M., Deen, B., Pitskel, N.B., Sugrue, D.R., Voos, A.C., et al., 2010. Neural signatures of autism. *Proceedings of the National Academy of Sciences*, 201010412.
- Kawahara, J., Brown, C.J., Miller, S.P., Booth, B.G., Chau, V., Grunau, R.E., Zwicker, J.G., Hamarneh, G., 2017. Brainnetcn: Convolutional neural networks for brain networks; towards predicting neurodevelopment. *NeuroImage* 146, 1038–1049.
- Kiar, G., Roncal, W.G., Mhembe, D., Bridgeford, E., Burns, R., Vogelstein, J., 2016. ndmg: Neurodatas mri graphs pipeline. *Zenodo*.
- Kingma, D.P., Ba, J.L., 2015. Adam: A method for stochastic optimization.
- Koshino, H., Carpenter, P.A., Minshew, N.J., Cherkassky, V.L., Keller, T.A., Just, M.A., 2005. Functional connectivity in an fmri working memory task in high-functioning autism. *Neuroimage* 24, 810–821.
- Lindquist, M., 2016. Dynamic connectivity: Pitfalls and promises.
- Lindquist, M.A., Xu, Y., Nebel, M.B., Caffo, B.S., 2014. Evaluating dynamic bivariate correlations in resting-state fmri: a comparison study and a new approach. *NeuroImage* 101, 531–546.
- Liu, Y., Liang, M., Zhou, Y., He, Y., Hao, Y., Song, M., Yu, C., Liu, H., Liu, Z., Jiang, T., 2008. Disrupted small-world networks in schizophrenia. *Brain* 131, 945–961.
- Lord, C., Risi, S., Lambrecht, L., Cook, E.H., Leventhal, B.L., DiLavore, P.C., Pickles, A., Rutter, M., 2000. The autism diagnostic observation schedule-generic: A standard measure of social and communication deficits associated with the spectrum of autism. *Journal of autism and developmental disorders* 30, 205–223.
- Lynch, C.J., Uddin, L.Q., Supekar, K., Khoutham, A., Phillips, J., Menon, V., 2013. Default mode network in childhood autism: posteromedial cortex heterogeneity and relationship with social deficits. *Biological psychiatry* 74, 212–219.
- Manton, J.H., Mahony, R., Hua, Y., 2003. The geometry of weighted low-rank approximations. *IEEE Transactions on Signal Processing* 51, 500–514.
- Menon, V., 2011. Large-scale brain networks and psychopathology: a unifying triple network model. *Trends in cognitive sciences* 15, 483–506.
- Mostofsky, S.H., Dubey, P., Jerath, V.K., Jansiewicz, E.M., Goldberg, M.C., Denckla, M.B., 2006. Developmental dyspraxia is not limited to imitation in children with autism spectrum disorders. *Journal of the International Neuropsychological Society* 12, 314–326.
- Muschelli, J., Nebel, M.B., Caffo, B.S., Barber, A.D., Pekar, J.J., Mostofsky, S.H., 2014. Reduction of motion-related artifacts in resting state fmri using a compcor. *Neuroimage* 96, 22–35.
- Nebel, M.B., Eloyan, A., Nettles, C.A., Sweeney, K.L., Ament, K., Ward, R.E., Choe, A.S., Barber, A.D., Pekar, J.J., Mostofsky, S.H., 2016. Intrinsic visual-motor synchrony correlates with social deficits in autism. *Biological psychiatry* 79, 633–641.
- Nebel, M.B., Joel, S.E., Muschelli, J., Barber, A.D., Caffo, B.S., Pekar, J.J., Mostofsky, S.H., 2014. Disruption of functional organization within the primary motor cortex in children with autism. *Human brain mapping* 35, 567–580.
- Niznikiewicz, M.A., Kubicki, M., Shenton, M.E., 2003. Recent structural and functional imaging findings in schizophrenia. *Current Opinion in Psychiatry* 16, 123–147.
- Nocedal, J., Wright, S., 2006. Numerical optimization. Springer Science & Business Media.
- Parisot, S., Ktena, S.I., Ferrante, E., Lee, M., Guerrero, R., Glocker, B., Rueckert, D., 2018. Disease prediction using graph convolutional networks: Application to autism spectrum disorder and alzheimers disease. *Medical image analysis* 48, 117–130.
- Park, C.h., Kim, S.Y., Kim, Y.H., Kim, K., 2008. Comparison of the small-world topology between anatomical and functional connectivity in the human brain. *Physica A: statistical mechanics and its applications* 387, 5958–5962.
- Penny, W.D., Friston, K.J., Ashburner, J.T., Kiebel, S.J., Nichols, T.E., 2011. Statistical parametric mapping: the analysis of functional brain images. Elsevier.
- Pouw, L.B., Rieffe, C., Stockmann, L., Gadow, K.D., 2013. The link between emotion regulation, social functioning, and depression in boys with asd. *Research in Autism Spectrum Disorders* 7, 549–556.
- Price, T., Wee, C.Y., Gao, W., Shen, D., 2014. Multiple-network classification of childhood autism using functional connectivity dynamics, in: *International Conference on Medical Image Computing and Computer-Assisted Intervention*, Springer. pp. 177–184.
- Propper, R.E., ODonnell, L.J., Whalen, S., Tie, Y., Norton, I.H., Suarez, R.O., Zollei, L., Radmanesh, A., Golby, A.J., 2010. A combined fmri and dti examination of functional language lateralization and arcuate fasciculus structure: effects of degree versus direction of hand preference. *Brain and cognition* 73, 85–92.
- Rabany, L., Brocke, S., Calhoun, V.D., Pittman, B., Corbera, S., Wexler, B.E., Bell, M.D., Pelphrey, K., Pearlson, G.D., Assaf, M., 2019. Dynamic functional connectivity in schizophrenia and autism spectrum disorder: Convergence, divergence and classification. *NeuroImage: Clinical* 24, 101966.
- Raichle, M.E., 2015. The brain's default mode network. *Annual review of neuroscience* 38, 433–447.
- Rashid, B., Damaraju, E., Pearlson, G.D., Calhoun, V.D., 2014. Dynamic connectivity states estimated from resting fmri identify differences among schizophrenia, bipolar disorder, and healthy control subjects. *Frontiers in human neuroscience* 8, 897.
- Rubinov, M., Sporns, O., 2010. Complex network measures of brain connectivity: uses and interpretations. *Neuroimage* 52, 1059–1069.
- Rudie, J.D., Brown, J., Beck-Pancer, D., Hernandez, L., Dennis, E., Thompson, P., Bookheimer, S., Dapretto, M., 2013. Altered functional and structural brain network organization in autism. *NeuroImage: clinical* 2, 79–94.
- Schnabel, R.B., Toint, P.L., 1983. Forcing sparsity by projecting with respect to a non-diagonally weighted frobenius norm. *Mathematical Programming* 25, 125–129.
- Sestieri, C., Corbetta, M., Romani, G.L., Shulman, G.L., 2011. Episodic memory retrieval, parietal cortex, and the default mode network: functional and topographic analyses. *Journal of Neuroscience* 31, 4407–4420.
- Skudlarski, P., Jagannathan, K., Calhoun, V.D., Hampson, M., Skudlarska, B.A., Pearlson, G., 2008. Measuring brain connectivity: diffusion tensor imaging validates resting state temporal correlations. *Neuroimage* 43, 554–561.
- Smith, S.M., Beckmann, C.F., Andersson, J., Auerbach, E.J., Bijsterbosch, J., Douaud, G., Duff, E., Feinberg, D.A., Griffanti, L., Harms, M.P., et al., 2013. Resting-state fmri in the human connectome project. *Neuroimage* 80, 144–168.
- Spitzer, R.L., Williams, J.B., 1980. Diagnostic and statistical manual of mental disorders, in: *American Psychiatric Association*, Citeseer.
- Sporns, O., Chialvo, D.R., Kaiser, M., Hilgetag, C.C., 2004. Organization, development and function of complex brain networks. *Trends in cognitive sciences* 8, 418–425.
- Sridharan, D., Levitin, D.J., Menon, V., 2008. A critical role for the right fronto-insular cortex in switching between central-executive and default-mode networks. *Proceedings of the National Academy of Sciences* 105, 12569–12574.
- Sui, J., He, H., Yu, Q., Rogers, J., Pearlson, G., Mayer, A.R., Bustillo, J., Calhoun, V.D., et al., 2013. Combination of resting state fmri, dti, and smri data to discriminate schizophrenia by n-way mcca+ jica. *Frontiers in human neuroscience* 7, 235.

- Sun, Y., Yin, Q., Fang, R., Yan, X., Wang, Y., Bezerianos, A., Tang, H., Miao, F., Sun, J., 2014. Disrupted functional brain connectivity and its association to structural connectivity in amnesic mild cognitive impairment and alzheimers disease. *PloS one* 9.
- Tzourio-Mazoyer, N., Landeau, B., Papathanassiou, D., Crivello, F., Etard, O., Delcroix, N., Mazoyer, B., Joliot, M., 2002. Automated anatomical labeling of activations in spm using a macroscopic anatomical parcellation of the mni mri single-subject brain. *Neuroimage* 15, 273–289.
- Uddin, L.Q., Yeo, B.T., Spreng, R.N., 2019. Towards a universal taxonomy of macro-scale functional human brain networks. *Brain topography* , 1–17.
- Van Essen, D.C., Smith, S.M., Barch, D.M., Behrens, T.E., Yacoub, E., Ugurbil, K., Consortium, W.M.H., et al., 2013. The wu-minn human connectome project: an overview. *Neuroimage* 80, 62–79.
- Van Essen, D.C., Ugurbil, K., Auerbach, E., Barch, D., Behrens, T., Bucholz, R., Chang, A., Chen, L., Corbetta, M., Curtiss, S.W., et al., 2012. The human connectome project: a data acquisition perspective. *Neuroimage* 62, 2222–2231.
- Venkataraman, A., Duncan, J.S., Yang, D.Y.J., Pelphrey, K.A., 2015. An unbiased bayesian approach to functional connectomics implicates social-communication networks in autism. *NeuroImage: Clinical* 8, 356–366.
- Venkataraman, A., Kubicki, M., Golland, P., 2012. From brain connectivity models to identifying foci of a neurological disorder, in: *International Conference on Medical Image Computing and Computer-Assisted Intervention*, Springer. pp. 715–722.
- Venkataraman, A., Kubicki, M., Golland, P., 2013. From connectivity models to region labels: identifying foci of a neurological disorder. *IEEE transactions on medical imaging* 32, 2078–2098.
- Venkataraman, A., Rathi, Y., Kubicki, M., Westin, C.F., Golland, P., 2011. Joint modeling of anatomical and functional connectivity for population studies. *IEEE transactions on medical imaging* 31, 164–182.
- Venkataraman, A., Wymbs, N., Nebel, M.B., Mostofsky, S., 2017. A unified bayesian approach to extract network-based functional differences from a heterogeneous patient cohort, in: *International Workshop on Connectomics in Neuroimaging*, Springer. pp. 60–69.
- Venkataraman, A., Yang, D.Y.J., Pelphrey, K.A., Duncan, J.S., 2016. Bayesian community detection in the space of group-level functional differences. *IEEE transactions on medical imaging* 35, 1866–1882.
- Visser, M.E., Cohen, M.X., Geurts, H.M., 2012. Brain connectivity and high functioning autism: a promising path of research that needs refined models, methodological convergence, and stronger behavioral links. *Neuroscience & Biobehavioral Reviews* 36, 604–625.
- Wang, F., Kalmar, J.H., He, Y., Jackowski, M., Chepenik, L.G., Edmiston, E.E., Tie, K., Gong, G., Shah, M.P., Jones, M., et al., 2009. Functional and structural connectivity between the perigenual anterior cingulate and amygdala in bipolar disorder. *Biological psychiatry* 66, 516–521.
- Wang, Q., Su, T.P., Zhou, Y., Chou, K.H., Chen, I.Y., Jiang, T., Lin, C.P., 2012. Anatomical insights into disrupted small-world networks in schizophrenia. *Neuroimage* 59, 1085–1093.
- Wee, C.Y., Yap, P.T., Zhang, D., Denny, K., Browndyke, J.N., Potter, G.G., Welsh-Bohmer, K.A., Wang, L., Shen, D., 2012. Identification of mci individuals using structural and functional connectivity networks. *Neuroimage* 59, 2045–2056.
- Weyandt, L., Swentosky, A., Gudmundsdottir, B.G., 2013. Neuroimaging and adhd: fmri, pet, dti findings, and methodological limitations. *Developmental neuropsychology* 38, 211–225.
- Whitwell, J.L., Avula, R., Master, A., Vemuri, P., Senjem, M.L., Jones, D.T., Jack Jr, C.R., Josephs, K.A., 2011. Disrupted thalamocortical connectivity in psp: a resting-state fmri, dti, and vbm study. *Parkinsonism & related disorders* 17, 599–605.
- Williams, D.L., Goldstein, G., Minshew, N.J., 2006. The profile of memory function in children with autism. *Neuropsychology* 20, 21.
- Zimmermann, J., Griffiths, J.D., McIntosh, A.R., 2018. Unique mapping of structural and functional connectivity on cognition. *Journal of Neuroscience* 38, 9658–9667.